ELASTO-VISCOPLASTIC WAVE PROPAGATION IN A SINGLE CRYSTALLOGRAPHIC SILICON THIN STRUCTURE

A Thesis

by

LI LIU

Submitted to the Office of Graduate Studies of
Texas A&M University
in partial fulfillment of the requirements for the degree of

MASTER OF SCIENCE

May 2005

Major Subject: Mechanical Engineering

ELASTO-VISCOPLASTIC WAVE PROPAGATION IN A SINGLE CRYSTALLOGRAPHIC SILICON THIN STRUCTURE

A Thesis

by

LI LIU

Submitted to Texas A&M University
in partial fulfillment of the requirements
for the degree of

MASTER OF SCIENCE

Approved as to style and content by:

Chii-Der S. Suh (Chair of Committee)	Andrew K. Chan (Member)
Arun R. Srinivasa (Member)	Dennis L. O'Neal (Head of Department)

May 2005

Major Subject: Mechanical Engineering

ABSTRACT

Elasto-Viscoplastic Wave Propagation in a Single Crystallographic Silicon Thin Structure. (May 2005)

Li Liu, B.S., Tsinghua University, Beijing, China;

M.S., Tsinghua University, Beijing, China

Chair of Advisory Committee: Dr. Chii-Der Suh

The thesis provides the required knowledge base for establishing Laser Induced Stress Wave Thermometry (LISWT) as a viable alternative to current infrared technologies for temperature measurement up to 1000°C with ±1°C resolution. The need for a non-contact, high resolution thermal measurement methodology applicable to Rapid Thermal Processing (RTP) motivated the work. A stress wave propagation model was developed and a complex, temperature-dependent elasto-viscoplastic constitutive law was identified. A stagger-grid finite difference scheme was followed to approximate the solution field subject to temperature and plate thickness variations. Extensive numerical experiments were conducted to identify the proper time and spatial steps. A Gabor wavelet transform scheme was also employed for the extraction of wafer thermal and geometric information from exploring wave attenuation and dispersion.

Researched results concluded that wave group velocity is a nonlinear function of temperature. Nonlinearity became more prominent at high temperatures and low frequencies. As such, for LISWT to achieve better thermal resolution at high temperatures, low frequency components of the induced stress wave should be exploited. The results also showed that the influence of temperature on attenuation is relatively small. It is not recommended to use attenuation for resolving temperature variation as small as several degrees Celsius. In addition to temperature, geometry also was found to have an impact on wave dispersion and attenuation. The results showed that the influence of thickness on wave velocity is significant, thus suggesting that for LISWT to achieve high temperature resolution, wafer thickness must be accurately calibrated in order to eliminate all possible errors introduced by thickness variation. The study

established the basic framework for LISWT to be applicable to silicon wafer RTP at elevated temperatures. The model and methods developed for the course of the research can be easily adapted to account for other nondestructive evaluation applications involving the use of surface, plate or bulk waves for material characterization and thermal profiling.

ACKNOWLEDGEMENTS

I would like to express my deepest gratitude to my thesis advisor, Dr. Chii-Der Suh, who guided me through the challenging process of conducting research and writing this thesis. This thesis would not have been possible without his invaluable advice and financial support. I am also grateful to my thesis committee members – Dr. Andrew Chan and Dr. Arun Srinivasa for their support. Finally I wish to thank my wife, Dongmin, for her love and understanding.

TABLE OF CONTENTS

Page

CHAPTER Page

LIST OF FIGURES

Page

Page

LIST OF TABLES

Page

CHAPTER I

INTRODUCTION

1.1 Overview

Stress wave propagation in single crystalline silicon is seeing important applications in the annealing of thin silicon wafers. During Rapid Thermal Processing (RTP) of 12" wafers, the required thermal measurement resolution is ±1°C over the range from room temperature to 1200°C [1]. Furthermore, access to silicon wafers during RTP is limited due to the nature of the process. A non-contact, non-invasive technique with desired thermal resolution is therefore needed. Laser Induced Stress Wave Thermometry (LISWT) [2] is such a technique that has demonstrated certain welcome potentials. LISWT employs a pulsed laser for triggering propagating stress waves in the wafer. If the energy of the laser beam is sufficient enough to diffuse through the wafer thickness, dispersive Lamb guided waves would be induced. Generated waveforms are acquired using a type of fiber-optic sensor known as the fiber-tip interferometer (FTI) and processed using time-frequency analysis tools to extract feature information indicative of thermal variation. There are two ways that temperature may affect wave propagation in silicon wafers. Firstly, the constitutive law of the silicon material is temperature dependent. Secondly, thermal stresses caused by temperature variation lead to the change of stress distribution in the field, resulting in the changes in wave propagation. Therefore changes in wave propagation characteristics are good indicators of temperature changes.

Single crystalline silicon behaves elastically in room temperature and becomes elasto-viscoplastic at elevated 1200°C. Thus wave propagation in silicon exhibits certain elastic-viscoplastic behaviors depending on the temperature considered. While

---

This thesis follows the style and format of Wave Motion.

extensive theoretical and experimental works can be found in the field of elasticity, few works on plastic wave propagation in single crystalline silicon were documented. A unified wave propagation model applicable to the above temperature range is needed. Availability of the model would help establish useful guidelines for employing LISWT for thermal-profiling silicon wafers. The thesis documents the effort for developing such a wave motion model. Physically the model is constructed using fundamental laws of solid mechanics including conservation of linear momentum, kinematics and constitutive law. Mathematically the model is formulated as a first-order hyperbolic system of equations. This model allows 3D elasto-viscoplastic wave propagation in silicon wafers to be studied as functions of temperature and wafer thickness.

Due to the inherent complexity, the developed wave model is difficult to be solved analytically. Among the many numerical schemes for solving wave equations, finite-difference is widely used for modeling wave motions in earthquake and oil exploration seismology, ocean acoustics, laboratory ultrasonics, and various nondestructive evaluation applications. While finite difference provides a straightforward approach for initial-boundary value problems involving wave motions, its successful implementation depends on the proper choice of simulation parameters such as the temporal and spatial integration steps. These considerations are essential for ensuring valid results and acceptable computational costs.

As aforementioned, the mechanical waves induced in the silicon wafer are Lamb waves if sufficient laser radiation energy is deposited. Lamb waves are dispersive, which means their spectral structure changes with time. This property can be realized as a dispersion curve in which the relation between wave velocity and frequency is defined. The impact of temperature on wave propagation can manifest itself as changes in dispersion. This is exactly the underlying physics upon which LISWT is based. Therefore choosing a proper time-frequency analysis tool is essential in this investigation. The purpose of time-frequency analysis is to resolve the temporal behavior of individual frequency component. There are many time-frequency analysis tools including Short-Time Fourier Transform (STFT), Wigner-Ville Distribution

(WVD), Wavelet Transform (WT) and the newly emerged Hilbert-Huang Algorithm. In this investigation, Gabor Wavelet Transform is adopted for its high resolution in the time-frequency domain.

1.2 Laser Induced Stress Wave Thermometry (LISWT)

Before the advent of LISWT, there were other techniques for monitoring the temperature of a silicon wafer undergoing RTP. Pyrometry is one of these traditional techniques that is also non-contact, thus meeting the limited access requirement for RTP. However, the problem with pyrometry is its low resolution. As pyrometry can only achieve a resolution level of ±5°C, it falls short of meeting the ±1°C requirement needed for processing 12" wafers at elevated temperatures. This difficulty is rooted in the physical principle on which it is based, rather than imperfections of instrumentation.

Other techniques such as the one described by Lee et al. [3] involve inducing and detecting stress waves using contact piezoelectric transducers. There are many disadvantages inherent of techniques requiring physical contact. First of all, using transducers for stress wave generation violates the non-contact requirement in RTP. Secondly, as it requires conversion from electrical to mechanical signals, using transducer for sensing wave motions may introduce non-negligible errors. Lastly, a transducer mechanically contacting a wafer inevitably constitutes a vigorous heat sink, which further aggravates thermal measurement with poor resolution and errors. These disadvantages limit fabrication yield, compromise productivity and delay turnaround time. In contrast, the LISWT technique is of non-contact, broadband generation and sensing and it can be operated remotely in-situ.

LISWT, as an emerging technology for silicon wafer thermal profiling, has seen rapid progress since its advent. The need for ±1°C thermal resolution for 12" wafer undergoing RTP motivated the pioneering research done by Rabroker, Suh and Vedantham [2, 4-8]. In their works, the feasibility of LISWT thermometry was demonstrated. They successfully showed, both experimentally and theoretically,

temperature measurement up to 600°C with ±2°C resolution. As stated, the key element in the LISWT technology is the stress wave propagating in the silicon wafer. Stress waves in the silicon at temperatures under 600°C are elastic. However, as the operation temperature in the RTP chamber increased from 25°C to exceeding 1000°C in a matter of seconds, the assumption of elasticity would not be valid for a rather wide range of temperatures. Derivation under the assumption of elasticity thus is invalid. Therefore, extension from elasticity to elasto-plasticity is essential for LISWT if it is to cover the full range of the RTP temperatures and be a valid alternative to the low-resolution pyrometric technique. The typical setup of the LISWT configuration is shown schematically in Fig. 1.

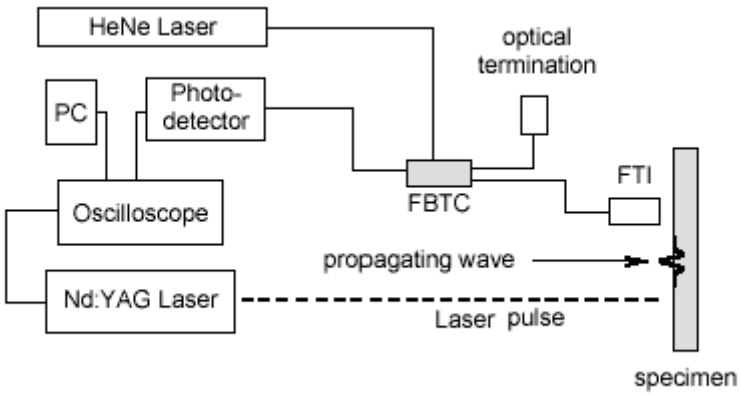

Fig 1.1 Experimental setup of a LISWT system (Adopted from [4])

1.3 Elasto-Viscoplastic Wave Propagation in Single Crystallographic Materials

Although the effort of modeling elasto-viscoplastic waves can be traced as far back as the 1960's [9], with the latest one published in late 2003 [10], there are very few publications that address elasto-viscoplastic waves in silicon at elevated temperatures. There are two key issues that need to be resolved before an elasto-viscoplastic wave propagation model can be developed. The first one is the kinematics of elastic-plastic

deformation. In literature, it is a common practice to calculate the total strain as the sum of the elastic strain and the plastic strain. However its kinematical implications must be clarified. Valid assumptions must be made to justify the simple summation operation. In the 1960's, Lee and Liu [9] presented an idea that laid the framework for research on elasto-plastic deformation. They assumed a fictitious elastically deformed state between the original (undeformed) state and the elasto-plastic state in order to calculate the displacement gradients and strains. A mathematically rigorous procedure was then followed for obtaining the elasto-plastic kinematics. The second one is the constitutive law of silicon material. All reviewed papers on plastic wave propagation adopt a fairly simple linear-elastic-perfect-plastic (LEPP) material model, which is not a true representation of silicon material property at elevated temperatures. Therefore the derivations and conclusions cannot be readily employed to meet the requirements of this research. Among researchers who have worked on the constitutive law of single crystal structures, Alexander and Haasen [11] proposed a constitutive model in the 1960's. Later this model was refined by Suezava et al. [12] and subsequently named after the principle inventors as the Haasen-Sumino model. In the 1980's, Tsai et al [13] generalized a 3D model using the Hassen-Sumino model. Tsai's model is supported by plenty of experimental data and therefore widely adopted by many researchers in this area. In this investigation, Tsai's model is used to define the viscoplastic constitutive law of single crystalline silicon at elevated temperatures. Since Tsai's model is derived from the uniaxial tension experiments, modifications are introduced to make it applicable to the study documented herein.

Mathematically, classic wave equations are second-order hyperbolic equations of displacement or stress. In this investigation, due to the complexity of the constitutive law, it is impossible to derive a second-order hyperbolic equation in terms of either displacements or stresses. Instead, a first order hyperbolic equation system is followed. Velocities and stresses are the dependent variables in the equation system. There are nine unknowns including three velocity components and six stress components in the equations that describe 3D wave motion [14]. There are two major advantages of the

technique. First, initial and boundary conditions are specified in terms of the dependent variables alone. No derivatives of the dependent variables are involved. Secondly, stresses or velocities are the immediate results of solving the equations. Note that in the displacement formulation, further calculations are needed to obtain stress components and in the stress formulation, numerical integrations are needed to obtain displacements. Reducing the number of numerical differentiation or integration can result in less error. This would also be a welcome feature in applications in which stresses or stress gradients are the primary variables of interests.

1.4 Numerical Methods and Wave Signal Processing Tools

Wave equations can be solved analytically only for a few cases where the constitutive law, geometry and boundary conditions are simple. In this study, due to the complexity of the constitutive law, the first-order equation system cannot be solved analytically. An extensive survey on the methods viable for solving wave problems is performed. Cerveny et al presented the ray theory in the 1970's [15]. It is a powerful tool and is still widely used in seismic wave propagation. However, the theory breaks down for low frequency. For LISWT, laser induced stress waves are broadband, so ray theory cannot apply. Other methods fall into two categories – one that solves wave equations in the strong formulation and one that solves the equations in the weak form. Finite element is an example of the former, which is preferred when geometry and boundary conditions are complex. Finite difference is a typical method of the latter category that is used by many researchers to solve wave problems [16-18].

Many enhancements have been introduced to increase the approximation accuracy for the finite difference method. Kasloff et al. proposed the pseudospectral method, which performs the space derivatives using Fourier transform and inverse Fourier transform [19,20]. Tal-Ezer [21] described a new method for approximating the time dependence of solutions using orthogonal polynomials involving powers of the spatial

differential operator of the equation. Recently Kole [22] presented a matrix exponential approach that is essentially the extension of Tal-Ezer's method.

As a strong form solution, finite difference is a straightforward approach to differential equations that is easy to implement. In non-axisymmetrical wave problems, comprehensive 3D solutions are sought. Due to the large number of unknowns involved (9 unknowns for each node in a 3D mesh), an algorithm that can be parallelized is highly desirable. Finite difference can be easily parallelized. This is probably why finite difference is prevailing in solving 3D wave problems [23]. In this investigation, an explicit staggered grid finite difference method is employed. The explicit method is adopted because the computational load could be too high for the implicit method. Although the explicit method is not unconditionally stable, the problem can be avoided by wisely choosing the time step [24].

The major drawback of finite difference, however, is its numerical dispersion. Reference [25] is referred for details on numerical dispersion. This disadvantage prevents finite difference from accurately predicting long distance wave propagation. To avoid numerical dispersion, appropriate time and spatial steps must be chosen. Besides all the aforementioned enhancements, numerical experiments can be helpful in determining the right finite difference parameters. In this study, a numerical experiment that includes three cases of different mesh sizes is conducted to study the influence of spatial steps on numerical dispersion so that spatial steps can be identified for 3D studies. The convergence of the results indicates the successful implementation of the finite difference scheme.

In LISWT where propagating waves are employed for thermal measurement, there are two key practical issues in implementation. One is data acquisition and the other is wave signal processing. Physically waveforms are acquired through an optical interferometer. In this study, a model is built to simulate the waveforms. After waveforms are obtained, through either experiments or simulations, a proper wave signal processing tool must be applied to extract thermal information. Fast Fourier Transform (FFT) is the most used tool in signal processing. However it is not effective for this

investigation because it can only provide spectral information without time information. FFT is usually applied to time-invariant signals whose frequency structure does not change with time. As alternatives to FFT, Short Time Fourier Transform (STFT) and Wavelet Transform (WT) can provide both time and frequency information. The newly emerged Hilbert-Huang Algorithm (HHA) for calculating instantaneous frequency provides higher resolution, though it is yet to be fully developed theoretically. Successful implementation of HHA is operator dependent. That is, a good estimation of the frequency components and the time variation of these components are essential for the successful application of the algorithm. Much preliminary work has been done using HHA. Nevertheless, due to the aforementioned problems, it is not chosen for the study. Wavelet Transform using Gaussian functions as the window functions is named Gabor Wavelet Transform (GWT). It provides the best resolution in the time-frequency domain. Therefore GWT is the time-frequency analysis tool employed for the reported investigation herein.

1.5 Research Objectives

The primary objective of the proposed research is to establish the knowledge base needed for demonstrating the feasibility of LISWT for high temperature applications, which is essential if LISWT is to be used in RTP chambers as an alternative to the pyrometric techniques. Stress wave propagation in silicon wafer at extreme temperatures will be analytically established and numerically modeled. The work is based on a unified constitutive law, which accurately embodies the elasto-viscoplastic characteristics of silicon wafer at temperatures ranging from 25°C to exceeding 1000°C. Specifically, the research establishes the correlation of temperature with the group velocity of spectral components (thus temperature dependent dispersion) over the targeted range of temperatures. In addition, a guideline for accurate temperature measurement is established.

Although the primary objective of this investigation is to understand temperature influence on wave propagation, the influence of other parameters such as wafer thickness is also studied. The finite difference program developed for the study can be easily modified to carry out simulations involving propagating stress waves in various other types of NDE applications.

CHAPTER II

THEORY OF ELASTO-VISCOPLASTIC WAVE PROPAGATION

2.1 Kinematics and Equation of Motion

2.1.1 Kinematics of elasto-plastic deformation

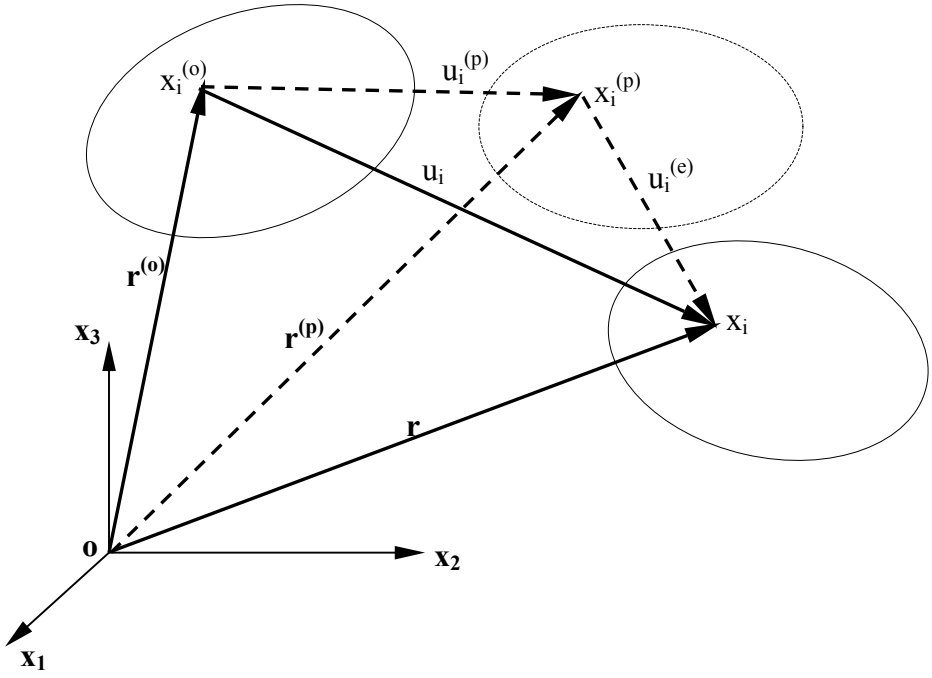

Fig. 2.1 The elasto-plastic deformation of a continuum

The various physical states of a body undergoing elastic-plastic deformation are schematically shown in Fig. 2.1. There are three configurations of the body -- the reference configuration, the relaxed configuration and the deformed configuration. The reference configuration defines the original position of material points in the body. It is the initial state of the body. The deformed configuration defines the position of material points at a particular moment when the body is subjected to a set of external forces. If

the plastically deformed body is released of all external forces, it will not bounce back to the original or undeformed configuration. Due to the plastic deformation, the body will come to a third configuration, which is the relaxed configuration shown in Fig. 2.1. The net difference between the reference configuration and the relaxed configuration is the plastic deformation.

In Fig. 2.1, $x_i^{(o)}(i=1,2,3)$ is the Cartesian coordinate of a generic point in the continuum in its reference configuration. $x_i^{(p)}(i=1,2,3)$ is the coordinate of the point in the relaxed configuration and $x_i(i=1,2,3)$ is the coordinate of the point in the deformed configuration. $u_i^{(e)}(i=1,2,3)$ is the component of elastic deformation along the *i*-direction, while $u_i^{(p)}(i=1,2,3)$ is the component of plastic deformation along the *i*-direction. Note that $r^{(o)}$, $r^{(p)}$ and r are the position vectors associated with their respective configurations. The following kinematics relations exist,

$$x_i = x_i^{(p)} + u_i^{(e)} \tag{2.1}$$

$$x_i + dx_i = x_i^{(p)} + dx_i^{(p)} + u_i^{(e)} + du_i^{(e)} \tag{2.2}$$

$$dx_i = dx_i^{(p)} + du_i^{(e)} \tag{2.3}$$

$$v_i = v_i^{(p)} + v_i^{(e)} \tag{2.4}$$

where $v_i(i=1,2,3)$ is the component of total deformation rate, $v_i^{(e)}(i=1,2,3)$ is the component of elastic deformation rate and $v_i^{(p)}(i=1,2,3)$ is the component of plastic deformation rate. Define the elastic velocity gradient tensor, $D_{ij}^{(e)} = \dfrac{\partial v_i^{(e)}}{\partial x_i^{(p)}}$. This definition is in accordance with Equation (2.1) or (2.4), which means the deformed configuration can be seen as the relaxed configuration plus the elastic deformation. Define the plastic velocity gradient tensor $D_{ij}^{(p)} = \dfrac{\partial v_i^{(p)}}{\partial x_j^{(p)}}$. The plastic constitutive law describes the change of the relaxed configuration with time, so the plastic velocity gradient tensor is defined in the relaxed configuration. Define the total velocity gradient

tensor, $D_{ij} = \frac{\partial v_i}{\partial x_j}$. Note that the total velocity gradient tensor is defined in the deformed configuration so that it complies with the equation of motion, which is derived in the deformed configuration. Using Eq. (2.4), the total velocity gradient tensor D_{ij} is defined as

$$D_{ij} = \frac{\partial v_i^{(p)}}{\partial x_j} + \frac{\partial v_i^{(e)}}{\partial x_j} \tag{2.5}$$

Apply the chain rule of partial differentials, the above total gradient tensor becomes

$$D_{ij} = \frac{\partial v_i^{(p)}}{\partial x_k^{(p)}} \frac{\partial x_k^{(p)}}{\partial x_j} + \frac{\partial v_i^{(e)}}{\partial x_k^{(p)}} \frac{\partial x_k^{(p)}}{\partial x_j} \tag{2.6}$$

Eq. (2.6) has the following equivalent form by applying the definitions of $D_{ij}^{(e)}$ and $D_{ij}^{(p)}$ as

$$D_{ij} = (D_{ik}^{(e)} + D_{ik}^{(p)}) \frac{\partial x_k^{(p)}}{\partial x_j} \tag{2.7}$$

From Eq. (2.1), Eq. (2.7) has the alternative form

$$D_{ij} = (D_{ik}^{(e)} + D_{ik}^{(p)})(\delta_{kj} - \frac{\partial u_k^{(e)}}{\partial x_j}) \tag{2.8}$$

For small elastic deformations, the multiplicative factor in the second parenthesis on the right hand side in Eq. (2.8) can be ignored. Thus Eq. (2.8) is further simplified as

$$D_{ij} = (D_{ik}^{(e)} + D_{ik}^{(p)}) \tag{2.9}$$

Note that all the above derivations comply with the notations of tensor summation. Eq. (2.9) states that, for small elastic deformation, the total velocity gradient tensor can be regarded as the summation of the elastic velocity gradient tensor and the plastic velocity gradient previously defined above.

Recall that the total strain rate and the elastic strain rate are, respectively,

$$\dot{\varepsilon}_{ij} = \frac{1}{2}(\frac{\partial v_i}{\partial x_j} + \frac{\partial v_j}{\partial x_i}), \tag{2.10}$$

and

$$\dot{\varepsilon}_{ij}^{(e)} = \frac{1}{2}\left(\frac{\partial v_i^{(e)}}{\partial x_j} + \frac{\partial v_j^{(e)}}{\partial x_i}\right). \tag{2.11}$$

From Eqs. (2.9), (2.10) and (2.11), the total strain becomes

$$\dot{\varepsilon}_{ij} = \dot{\varepsilon}_{ij}^{(e)} + \frac{1}{2}\left(D_{ij}^{(p)} + D_{ji}^{(p)}\right). \tag{2.12}$$

Note that Eq (2.12) defines the kinematics relation of elasto-plastic deformation in which the second term on the right hand side is the plastic strain rate, $\dot{\varepsilon}_{ij}^{(p)} = \frac{1}{2}\left(D_{ij}^{(p)} + D_{ji}^{(p)}\right)$.

2.1.2 Equation of Motion

The linear equation of motion in Eq. (2.13) is derived from the conservation of linear momentum,

$$\sigma_{ij,i} + f_j = \rho \ddot{u}_j, \tag{2.13}$$

where f_j is the $j-th$ component of the body force and u_j is the $j-th$ component of the displacement. The angular equation of motion below is derived from the conservation of angular momentum, which states that the stress tensor is symmetric,

$$\sigma_{ij} = \sigma_{ji}. \tag{2.14}$$

2.2 Constitutive Model of Silicon at Elevated Temperatures

2.2.1 Orthotropic material property of single crystal silicon in the elastic zone

Material orthotropy of single crystal silicon is the result of the cubic nature of its lattice. An orthotropic material has three orthogonal planes of symmetry. The stiffness matrix of such a material has nine independent material constants. If the coordinate axes are chosen to be aligned with the three planes of symmetry, the compliance matrix of the

orthotropic material will take the form in Eq. (2.15) below, with some of the entries being zeros. In general, if the coordinate axes are not aligned with the three planes of symmetry, there will not be entries that are zeros, though they can always be related to nine independent quantities.

Matrix entries in Eq. (2.15) can be written in terms of elastic constants, as shown in Eq. (2.16). In Eq. (2.16), there are 12 quantities: $E_{11}, E_{22}, E_{33}, \upsilon_{12}, \upsilon_{21}, \upsilon_{13}, \upsilon_{31}, \upsilon_{23}, \upsilon_{32}, G_{23}$ and G_{31}. Since the stiffness matrix is symmetric and as a result these quantities must comply with the Cauchy Relation defined in Eqs. (2.17a)-(2.17b), the number of independent quantities is nine.

$$C = \begin{bmatrix} C_{11} & C_{12} & C_{13} & 0 & 0 & 0 \\ C_{21} & C_{22} & C_{23} & 0 & 0 & 0 \\ C_{31} & C_{32} & C_{33} & 0 & 0 & 0 \\ 0 & 0 & 0 & C_{44} & 0 & 0 \\ 0 & 0 & 0 & 0 & C_{55} & 0 \\ 0 & 0 & 0 & 0 & 0 & C_{66} \end{bmatrix} \tag{2.15}$$

$$C = \begin{bmatrix} \frac{1}{E_{11}} & -\frac{\upsilon_{21}}{E_{22}} & -\frac{\upsilon_{31}}{E_{33}} & 0 & 0 & 0 \\ -\frac{\upsilon_{12}}{E_{11}} & \frac{1}{E_{22}} & -\frac{\upsilon_{32}}{E_{33}} & 0 & 0 & 0 \\ -\frac{\upsilon_{13}}{E_{11}} & -\frac{\upsilon_{23}}{E_{22}} & \frac{1}{E_{33}} & 0 & 0 & 0 \\ 0 & 0 & 0 & \frac{1}{2G_{23}} & 0 & 0 \\ 0 & 0 & 0 & 0 & \frac{1}{2G_{31}} & 0 \\ 0 & 0 & 0 & 0 & 0 & \frac{1}{2G_{12}} \end{bmatrix} \tag{2.16}$$

$$\frac{\upsilon_{21}}{E_{22}} = \frac{\upsilon_{12}}{E_{11}} \tag{2.17a}$$

$$\frac{\upsilon_{31}}{E_{33}} = \frac{\upsilon_{13}}{E_{11}} \tag{2.17b}$$

$$\frac{\upsilon_{32}}{E_{33}} = \frac{\upsilon_{23}}{E_{22}} \tag{2.17c}$$

The stiffness matrix is the inverse of the compliance matrix. Since most semiconductors are fabricated using 100 wafers, the stiffness matrix of 100 wafer at room temperature is given in Eq. (2.18). The validity of Eq. (2.18) requires the alignment of coordinates with the direction of crystal growth in the silicon growing process.

$$E = \begin{bmatrix} 1.6564 & 0.6394 & 0.6394 & 0 & 0 & 0 \\ 0.6394 & 1.6564 & 0.6394 & 0 & 0 & 0 \\ 0.6394 & 0.6394 & 1.6564 & 0 & 0 & 0 \\ 0 & 0 & 0 & 0.7951 & 0 & 0 \\ 0 & 0 & 0 & 0 & 0.7951 & 0 \\ 0 & 0 & 0 & 0 & 0 & 0.7951 \end{bmatrix} \times 10^{11}(Pa) \tag{2.18}$$

The elastic constants, E_{ij}, in the stiffness matrix are functions of temperature. Empirical equations for calculating the influence of temperature on E_{ij} can be found in [26] as follows

$$E_{11} = 1.6564 \times 10^{12} \exp[-9.4 \times 10^{-5}(T - 298.15)](Pa) \tag{2.19a}$$

$$E_{12} = 0.6394 \times 10^{12} \exp[-9.8 \times 10^{-5}(T - 298.15)](Pa) \tag{2.19b}$$

$$E_{13} = 0.6394 \times 10^{12} \exp[-9.8 \times 10^{-5}(T - 298.15)](Pa) \tag{2.19c}$$

$$E_{23} = 0.6394 \times 10^{12} \exp[-9.8 \times 10^{-5}(T - 298.15)](Pa) \tag{2.19d}$$

$$E_{44} = 0.7915 \times 10^{12} \exp[-8.3 \times 10^{-5}(T - 298.15)](Pa) \tag{2.19e}$$

$$E_{55} = 0.7915 \times 10^{12} \exp[-8.3 \times 10^{-5}(T - 298.15)](Pa) \tag{2.19f}$$

$$E_{66} = 0.7915 \times 10^{12} \exp[-8.3 \times 10^{-5}(T - 298.15)](Pa) \tag{2.19g}$$

2.2.2 Viscoplastic behavior of single crystal silicon at elevated temperature

Single crystal silicon is brittle at room temperature. Before brittle facture would take place, single crystal silicon essentially obeys the Hooke's Law and behaves elastically. However, many experiments have showed that at temperatures between 520˚C and 600˚C, the transition from brittle to ductile behavior takes place [27]. At temperature above 600˚C, plastic behavior would become prominent. Or more accurately, single crystalline silicon would behave like a viscoplastic material because the governing constitutive law is rate dependent, as can be seen in the followings.

The plastic deformation of single crystalline silicon heavily depends on the dislocations in lattice. During the silicon growth process, thermal stress may cause the disarrangement of atoms in lattices. These disarrangements of atoms, known as dislocations, play a central role in the plastic deformation of single crystals such as single crystalline silicon. Dislocation density is the quantity that describes dislocations. It is defined as the length of dislocations per unit volume in the crystal. In the 1960's and 1970's, Haasen and Sumino [11,12], among others, studied the relation between plastic flow and dislocation density using uniaxial tension specimens and obtained an empirical constitutive law for silicon at elevated temperatures. Later this model was generalized by Tsai [13] to consider 3D loading. The Haasen-Sumino model is the most widely used constitutive law of single crystalline silicon that can be applied to temperature up to 1200˚C. The one dimensional Haasen-Sumino model is briefly described below.

The plastic strain rate is a function of dislocation density and dislocation velocity,

$$\dot{\varepsilon}_{ij}^{(p)} = N_m V b \tag{2.20}$$

where N_m is the dislocation density, V is the dislocation velocity and b is the magnitude of the Burgers vector. During the plastic deformation process, the dislocation density changes according to

$$\dot{N}_m = \delta N_m V \tag{2.21}$$

where δ is a built-in parameter whose value can be calculated using

$$\delta = K\tau_{eff}^{\lambda} = K(\tau_a - D\sqrt{N_m})^{\lambda} \tag{2.22}$$

with τ_{eff} being the effective stress, τ_a the applied stress, K and λ material constants and

$$D = \frac{Gb}{\beta}, \tag{2.23}$$

where G is shear modulus and β is a parameter characterizing the interaction between dislocations.

The dislocation velocity is determined by

$$V = V_0(\tau_a - D\sqrt{N_m})^h \tag{2.24}$$

where h is a material constant and

$$V_0 = (\frac{B_0}{\tau_0^p})\exp(-\frac{Q}{kT}), \tag{2.25}$$

in which B_0 is mobility, τ_0 is a material constant, Q is Peierls potential and T is temperature. Note that the presence of temperature in Eq. (2.25) realizes temperature dependent stress-strain and dislocation-strain relations.

Tsai [13] modified the above model to accommodate complex stress states. In Tsai's model, the second invariant of stress replaces the applied stress in the one-dimensional case. The plastic strain tensor is expressed as

$$\dot{\varepsilon}_{ij}^{(p)} = fS_{ij} \tag{2.26}$$

where S_{ij} is the deviatoric stress tensor and

$$f = \frac{bV_0N_m(\sqrt{J_2} - D_m\sqrt{N_m} - \tau_d)^h}{\sqrt{J_2}} \tag{2.27}$$

In Eq. (2.26), all parameters are defined as in the one-dimensional case. J_2 is the second invariant of the deviatoric stress tensor. In the 3D case, the dislocation density is determined by the following equation

$$\dot{N}_m = KV_0 N_m (\sqrt{J_2} - D_m \sqrt{N_m})^{h+\lambda}. \tag{2.28}$$

Eqs. (2.26)-(2.28) state the constitutive law of viscoplastic deformation of single crystalline silicon.

2.3 First-order Hyperbolic Equation System of 3D Wave Propagation

The physical phenomenon of wave propagation can be described mathematically by a second-order hyperbolic equation known as the displacement formulation or stress formulation. One of the disadvantages of the displacement formulation is that the stress is not solved directly from the wave equation. Rather, it is calculated through some post-processing procedures after the displacement is obtained, thus risk introducing approximation errors for stresses. In this study, an alternative way of describing wave propagation is presented. The idea is to combine the linear equation of motion, the kinematics relation and the constitutive law into an equation system, rather than one second-order equation in terms of displacements or stresses as in the conventional approach. First, replace displacement by velocity in the linear equation of motion and consider its component form.

$$\rho \frac{\partial v_1}{\partial t} = \frac{\partial \sigma_{11}}{\partial x_1} + \frac{\partial \sigma_{21}}{\partial x_2} + \frac{\partial \sigma_{31}}{\partial x_3} \tag{2.29}$$

$$\rho \frac{\partial v_2}{\partial t} = \frac{\partial \sigma_{12}}{\partial x_1} + \frac{\partial \sigma_{22}}{\partial x_2} + \frac{\partial \sigma_{32}}{\partial x_3} \tag{2.30}$$

$$\rho \frac{\partial v_3}{\partial t} = \frac{\partial \sigma_{13}}{\partial x_1} + \frac{\partial \sigma_{23}}{\partial x_2} + \frac{\partial \sigma_{33}}{\partial x_3} \tag{2.31}$$

Then, combining the kinematics relation in Eq. (2.12), Hooke's Law and viscoplastic law in Eq. (2.26) into their component form, one has the following equations

$$\frac{\partial v_1}{\partial x_1} = C_{11} \frac{\partial \sigma_{11}}{\partial t} + C_{12} \frac{\partial \sigma_{21}}{\partial t} + C_{13} \frac{\partial \sigma_{31}}{\partial t} + \frac{1}{2}(\sigma_{11} - \frac{\sigma_{11} + \sigma_{22} + \sigma_{33}}{3}) f \tag{2.32}$$

$$\frac{\partial v_2}{\partial x_2} = C_{21}\frac{\partial \sigma_{12}}{\partial t} + C_{22}\frac{\partial \sigma_{22}}{\partial t} + C_{23}\frac{\partial \sigma_{32}}{\partial t} + \frac{1}{2}(\sigma_{22} - \frac{\sigma_{11}+\sigma_{22}+\sigma_{33}}{3})f \tag{2.33}$$

$$\frac{\partial v_3}{\partial x_3} = C_{31}\frac{\partial \sigma_{13}}{\partial t} + C_{32}\frac{\partial \sigma_{23}}{\partial t} + C_{33}\frac{\partial \sigma_{33}}{\partial t} + \frac{1}{2}(\sigma_{33} - \frac{\sigma_{11}+\sigma_{22}+\sigma_{33}}{3})f \tag{2.34}$$

$$\frac{\partial v_1}{\partial x_2} + \frac{\partial v_2}{\partial x_1} = 2(C_{11}\frac{\partial \sigma_{12}}{\partial t} + C_{12}\frac{\partial \sigma_{22}}{\partial t} + C_{13}\frac{\partial \sigma_{32}}{\partial t}) + \sigma_{12}f \tag{2.35}$$

$$\frac{\partial v_1}{\partial x_3} + \frac{\partial v_3}{\partial x_1} = 2(C_{11}\frac{\partial \sigma_{13}}{\partial t} + C_{12}\frac{\partial \sigma_{23}}{\partial t} + C_{13}\frac{\partial \sigma_{33}}{\partial t}) + \sigma_{13}f \tag{2.36}$$

$$\frac{\partial v_2}{\partial x_3} + \frac{\partial v_3}{\partial x_2} = 2(C_{21}\frac{\partial \sigma_{13}}{\partial t} + C_{22}\frac{\partial \sigma_{23}}{\partial t} + C_{23}\frac{\partial \sigma_{33}}{\partial t}) + \sigma_{23}f \tag{2.37}$$

A close examination shows that these equations involve only the first-order derivatives in terms of time or spatial coordinates. Therefore a first-order equation system is obtained. The dependent variables are no longer displacements or stresses only. Instead it combines velocities and stresses altogether as the variables, as shown in Eq. (2.38) below where the variable is represented by a 9-element vector.

$$\mathbf{U} = [v_1, v_2, v_3, \sigma_{11}, \sigma_{12}, \sigma_{13}, \sigma_{22}, \sigma_{23}, \sigma_{33}]^T \tag{2.38}$$

A first-order differential equation in terms of this vector is used to replace the conventional second-order hyperbolic equation. Since it is still a description of wave propagation, it is of hyperbolic type. The advantages of this formulation are many folds. One is that the aforementioned problem of approximation errors can be alleviated. Another is that it is the only feasible way when the constitutive law is so complicated that eliminating variables to reduce the total number of equations becomes impossible. The viscoplastic constitutive law presented in Section 2.2.2 is exactly such a case.

In Eq. (2.38), v_i is the $i-th$ component of the velocity. Through proper manipulation, the above equations can be presented in the following matrix form with variable $\mathbf{U}$.

$$\mathbf{A}\frac{\partial \mathbf{U}}{\partial t} + \mathbf{B}\frac{\partial \mathbf{U}}{\partial x_1} + \mathbf{C}\frac{\partial \mathbf{U}}{\partial x_2} + \mathbf{D}\frac{\partial \mathbf{U}}{\partial x_3} + \mathbf{E} = \mathbf{0} \tag{2.39}$$

This is the first-order hyperbolic system used in this investigation. The matrices $\mathbf{A}$, $\mathbf{B}$, $\mathbf{C}$, $\mathbf{D}$ and vector $\mathbf{E}$ are defined below.

$$\mathbf{A} = \begin{bmatrix} -\rho & 0 & 0 & 0 & 0 & 0 & 0 & 0 & 0 \\ 0 & -\rho & 0 & 0 & 0 & 0 & 0 & 0 & 0 \\ 0 & 0 & -\rho & 0 & 0 & 0 & 0 & 0 & 0 \\ 0 & 0 & 0 & C_{11} & 0 & 0 & C_{12} & C_{13} & 0 \\ 0 & 0 & 0 & 0 & 2C_{12} & 0 & 2C_{11} & 0 & 2C_{13} \\ 0 & 0 & 0 & 0 & 0 & 2C_{13} & 0 & 2C_{11} & 2C_{12} \\ 0 & 0 & 0 & 0 & 0 & 2C_{23} & 0 & 2C_{21} & 2C_{22} \\ 0 & 0 & 0 & 0 & C_{22} & 0 & C_{21} & 0 & C_{23} \\ 0 & 0 & 0 & 0 & 0 & C_{33} & 0 & C_{31} & C_{32} \end{bmatrix} \tag{2.40}$$

$$\mathbf{B} = \begin{bmatrix} 0 & 0 & 0 & 1 & 0 & 0 & 0 & 0 & 0 \\ 0 & 0 & 0 & 0 & 0 & 0 & 1 & 0 & 0 \\ 0 & 0 & 0 & 0 & 0 & 0 & 0 & 1 & 0 \\ -1 & 0 & 0 & 0 & 0 & 0 & 0 & 0 & 0 \\ 0 & -1 & 0 & 0 & 0 & 0 & 0 & 0 & 0 \\ 0 & 0 & -1 & 0 & 0 & 0 & 0 & 0 & 0 \\ 0 & 0 & 0 & 0 & 0 & 0 & 0 & 0 & 0 \\ 0 & 0 & 0 & 0 & 0 & 0 & 0 & 0 & 0 \\ 0 & 0 & 0 & 0 & 0 & 0 & 0 & 0 & 0 \end{bmatrix} \tag{2.41}$$

$$\mathbf{C} = \begin{bmatrix} 0 & 0 & 0 & 0 & 0 & 0 & 1 & 0 & 0 \\ 0 & 0 & 0 & 0 & 1 & 0 & 0 & 0 & 0 \\ 0 & 0 & 0 & 0 & 0 & 0 & 0 & 0 & 1 \\ 0 & 0 & 0 & 0 & 0 & 0 & 0 & 0 & 0 \\ -1 & 0 & 0 & 0 & 0 & 0 & 0 & 0 & 0 \\ 0 & 0 & 0 & 0 & 0 & 0 & 0 & 0 & 0 \\ 0 & 0 & -1 & 0 & 0 & 0 & 0 & 0 & 0 \\ 0 & -1 & 0 & 0 & 0 & 0 & 0 & 0 & 0 \\ 0 & 0 & 0 & 0 & 0 & 0 & 0 & 0 & 0 \end{bmatrix} \tag{2.42}$$

$$\mathbf{D} = \begin{bmatrix} 0 & 0 & 0 & 0 & 0 & 0 & 0 & 1 & 0 \\ 0 & 0 & 0 & 0 & 0 & 0 & 0 & 0 & 1 \\ 0 & 0 & 0 & 0 & 0 & 1 & 0 & 0 & 0 \\ 0 & 0 & 0 & 0 & 0 & 0 & 0 & 0 & 0 \\ 0 & 0 & 0 & 0 & 0 & 0 & 0 & 0 & 0 \\ -1 & 0 & 0 & 0 & 0 & 0 & 0 & 0 & 0 \\ 0 & -1 & 0 & 0 & 0 & 0 & 0 & 0 & 0 \\ 0 & 0 & 0 & 0 & 0 & 0 & 0 & 0 & 0 \\ 0 & 0 & -1 & 0 & 0 & 0 & 0 & 0 & 0 \end{bmatrix} \tag{2.43}$$

$$\mathbf{E} = [0 \quad 0 \quad 0 \quad \frac{1}{2}(\sigma_{11} - \frac{\sigma_{11}+\sigma_{22}+\sigma_{33}}{3}) \quad \sigma_{12}f \quad \sigma_{13}f \quad \sigma_{23}f \quad \frac{1}{2}(\sigma_{22} - \frac{\sigma_{11}+\sigma_{22}+\sigma_{33}}{3}) \quad \frac{1}{2}(\sigma_{33} - \frac{\sigma_{11}+\sigma_{22}+\sigma_{33}}{3})]^T \tag{2.44}$$

2.4 Summary

In this chapter, the kinematics of plastic deformation, the viscoplastic constitutive law of single crystalline silicon at elevated temperature and the governing equation of elasto-viscoplastic wave propagation were presented. On the assumption of small deformations, the kinematics of plastic deformation states that the total strain rate is the sum of elastic strain rate and plastic strain rate. The material orthotropy of single crystalline silicon in the elastic zone is characterized by its stiffness matrix with twelve material constants. Since these twelve constants must comply with the Cauchy Relation, the number of independent constants is nine. The viscoplastic constitutive law of single crystal silicon was adopted from Haasen-Sumino's and Tsai's models, with the latter describing the relation between plastic flows and 3D deviatoric stresses. Based on kinematics, constitutive law and the equation of motion of continuum, a first-order hyperbolic system of equations was derived which governs the 3D elasto-viscoplastic wave motion. Due to the complexity of the constitutive law, it is difficult to find an analytical solution to the system of equations. In Chapter IV, a finite difference scheme

is introduced for solving the equations numerically to obtain waveforms at selected locations in a 3D model domain.

CHAPTER III

WAVE ATTENUATION AND DISPERSION

In this chapter, the basic concepts of attenuation and dispersion are introduced. An attenuation factor, Q, is defined to quantify attenuation. Since attenuation depends on frequency and the Lamb waves induced by laser impulse in silicon wafers are broadband, a decomposing process has to be performed. Traditional Fourier Transform is not applicable because of the dispersive nature of Lamb waves. Instead, the projection of Gabor Wavelet Transform on the frequency axis is employed for determining the attenuation factor Q. Wave velocity dependence on wavenumber or frequency is called wave dispersion. The dispersion of elasto-viscoplastic waves propagating in silicon wafers is caused by both the wafer geometry and plastic behavior of the material. The dispersion curve is determined by the characteristic equation with elastic and plastic constants included. Any change of these constants results in the shifting of the dispersion curve. Since temperature has an influence on these constants, wave dispersion curve can be a good indicator of temperature and thickness variations.

3.1 Attenuation of Elasto-Viscoplastic Wave Propagation

3.1.1 Attenuation of mono-frequency wave

One-dimensional wave propagation in a homogeneous, elastic media is governed by a second-order hyperbolic equation as follows,

$$\frac{\partial^2 \xi}{\partial t^2} = \frac{E}{\rho}\frac{\partial^2 \xi}{\partial x^2} \tag{3.1}$$

where E is the Young's modulus and ρ is the density of the media. ξ is the dependent variable that can be displacement or stress. The general solution to Eq. (3.1) is a harmonic wave propagating in the x-direction, which is represented in the complex form

$$\xi = A \cdot \exp[i(kx - \omega t)] \tag{3.2}$$

In Eq. (3.2), k is the wave number and ω is the angular frequency. For purely elastic wave propagation governed by Eq. (3.1), k is a real number. Since A is constant, the amplitude of the wave remains constant.

If the media in which the wave propagates is not purely elastic, but rather displays characteristics of viscous damping, Eq. (3.1) needs to be modified to include the damping term. Consider displacement as the dependent variable, the modified equation is now

$$\rho \frac{\partial^2 y}{\partial t^2} = E \frac{\partial^2 y}{\partial x^2} - c \frac{\partial y}{\partial t} \tag{3.3}$$

where y is the displacement variable and c is the viscous damping coefficient. The solution to Eq. (3.3) is a little different from Eq. (3.2)

$$y = A \cdot \exp[i(\tilde{k}\, x - \omega t)] \tag{3.4}$$

The wave number $\tilde{k}$ is no longer a real number. Instead it is a complex number with real and imaginary parts as follows

$$\tilde{k} = k_1 + k_2 i \tag{3.5}$$

From Eqs. (3.4) and (3.5), the solution to Eq. (3.3) can be written as

$$y = A \cdot \exp(-k_2 x) \exp[i(k_1 x - \varpi t)] \tag{3.6}$$

While the second exponential term in Eq. (3.6) still indicates a wave propagating in the x-direction, the first exponential term with a multiplier A is now the amplitude of the wave. The wave is no longer harmonic. Note that the amplitude is now a function of the spatial coordinate x. Further examination shows that the amplitude decreases in the direction of wave propagating due to the negative sign in the $\exp(-k_2 x)$ term. This is one simple example of wave attenuation. In this case, attenuation is caused by the viscous damping in the material. The wave energy is dissipated so that the amplitude of the wave decreases accordingly. In other cases, attenuation can take place even in elastic media. Imagine a sphere wave propagating from a point source. Since the area

of wave front increases as the distance from the source becomes larger, the energy density of the wave front drops, resulting in continuously decreased amplitudes. Therefore, wave attenuation, characterized by decreasing wave amplitude, is the result of energy density loss due to physical or spatial reasons.

A logical way of evaluating attenuation is to compare the amplitude of the same wave at two different locations in space. Consider two subsequent locations x_1 and x_2 (where $x_1 > 0$ and $x_2 > 0$) in the propagation path of the wave governed by Eq. (3.3). The amplitudes at the two locations are

$$A_1 = A \cdot \exp(-k_2 x_1) \tag{3.7}$$

and

$$A_2 = A \cdot \exp(-k_2 x_2) \tag{3.8}$$

Define Q as the ratio between A_2 and A_1, thus

$$Q = \frac{A_2}{A_1} = \exp[-k_2 (x_2 - x_1)] \tag{3.9}$$

From Eq. (3.9), the quantity Q is determined by the distance between the two locations and k_2. This is a valid measurement of attenuation as it considers the influence of both medium material property and propagation length.

3.1.2 Elasto-viscoplastic wave attenuation in plates

While the discussion above is valid for wave propagation described by Eq. (3.4), Eq. (3.9) cannot be applied directly in this investigation of elasto-viscoplastic wave propagation. The reason is that Eq. (3.4) represents a mono-component wave. The elasto-viscoplastic waves in thin wafer structures are both broadband with multitudes of frequencies. The wavenumber of these waves is no longer a constant. Instead it is a function of frequency. Since k_2 is a function of frequency, Eq. (3.9) indicates that the attenuation of elasto-viscoplastic waves in a plate structure is a function of frequency. Therefore, before Eq. (3.9) can be applied, the wave has to be decomposed into mono-

frequency components. There are many ways to perform the decomposition. In this study, a method based on the Gabor Wavelet Transform (GWT) has been followed. GWT is to be treated in Chapter IV. The method is to perform GWT first and then find the maximum GWT value for a particular frequency along the time axis. The latter part is done through projecting the result of GWT on the frequency axis. Details of the methods are elaborated using the example signal in Fig. 3.1a which has 1 Hz and 2 Hz as its two frequency components. It can be seen in Fig. 3.1b that the projection of GWT coefficients unto the frequency axis looks similar to the Fourier Transform found in Fig. 3.1c. However, since Fourier Transform is not applicable in the case of dispersive waves, using projection of GWT is an alternative tool for studying Lamb wave attenuation.

Attenuation in dispersive waves can be calculated following the procedure below. Assume that $y_1(x_1,t)$ and $y_2(x_2,t)$ are the waveforms acquired at two different locations in space. $G_1(\omega)$ and $G_2(\omega)$ are the GWT projection of the two waveforms. The attenuation factor Q can be defined using

$$Q = -20 * \log[\frac{G_2(\omega)}{G_2(\omega)}] \tag{3.10}$$

The unit of the logarithmic operation Q is dB. Obviously Q is a function of frequency. Implicitly, since $G_1(\omega)$ and $G_2(\omega)$ are functions of locations x_1 and x_2, respectively, Q is also a function of the distance between the two locations. In elasto-viscoplastic wave propagation in plates, energy loss due to plastic deformation leads to wave attenuation. Since temperature has an immediate impact on plastic constitutive law, wave attenuation is an indicative function for temperature variation.

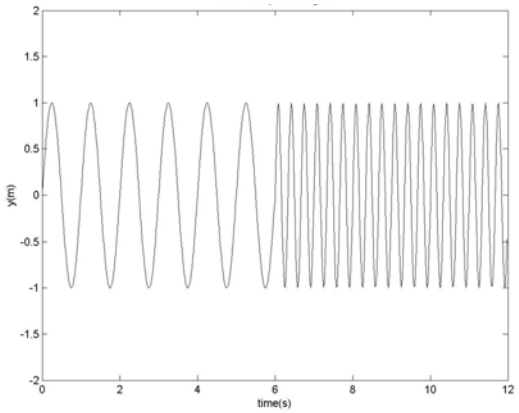

Fig. 3.1a 2-component signal

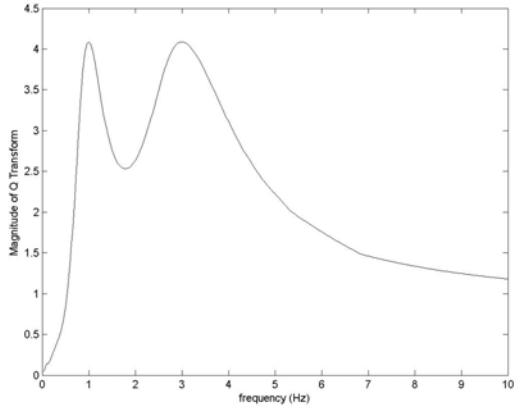

Fig. 3.1b Projection of GWT coefficients of the signal

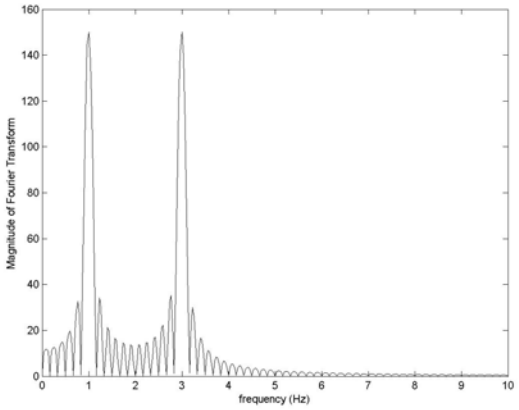

Fig. 3.1c FT of the signal

3.2 Dispersion of Elasto-Viscoplastic Lamb Waves

3.2.1 Wave dispersion

The concept of dispersion can also be introduced using a one-dimensional example. Consider a string on an elastic foundation. The wave propagating in the string can be described by

$$T\frac{\partial^2 y}{\partial x^2} - \mu y = \rho\frac{\partial^2 y}{\partial t^2} \tag{3.11}$$

where T is the tension in the string, μ is the elastic constant of the elastic foundation and ρ is the mass density of the string. Define $c_0 = \sqrt{T/P}$. The solution to Eq. (3.11) also takes the form of Eq. (3.2)

$$y = A\cdot\exp[i(kx-\omega t)] \tag{3.12}$$

However, the wavenumber, k, is no longer a constant. Instead it is a function of the angular frequency ω. Their relation is described by

$$k^2 = \frac{\omega^2}{c^2} - \frac{\mu}{T} \tag{3.13}$$

Recall that in the propagation of harmonic waves, the wave velocity, c, is defined as $c = \frac{\omega}{k}$. For the case at hand, the same calculation can be applied but it is no longer simply called wave velocity. Instead it is called the phase velocity. The phase velocity, c, of a wave propagating in a string on an elastic foundation can be calculated by

$$c = c_0 \sqrt{1 + \frac{\mu}{T} k^2} \tag{3.14}$$

From Eqs. (3.13) and (3.14), it can be seen that the wave propagating in a string on elastic foundation has phase velocity that is a function of frequency. The physical implication is that a particular component of the wave with frequency ω can only propagate at a velocity determined by Eq. (3.14). Consider an impulse excitation at a certain location on the string. An impulse is a broadband signal with many frequencies. Since different frequency components propagate at different velocities, the components become more and more out of phase as the signal propagates outwards. The result is htat at some location that is far away from the excitation, the waveform is no longer an impulse. Rather it is distorted. This phenomenon in wave propagation is called dispersion.

Next a simple example is used to illustrate the distortion effect. Consider a one-dimensional wave signal $y_1(x,t)$ that propagates in the positive x direction and contains two components with different frequency and velocity as follows

$$y_1(x,t) = \sin(x - 6.28t) + \sin(2x - 3.14t) \tag{3.15}$$

The waveforms at $t = 0$ and $t = 5.0$ are shown in Fig. 3.2. Distortion of the waveform is obvious.

As a comparison, a nondispersive wave $y_2(x,t)$ that contains two components with different frequency but same velocity is considered,

$$y_2(x,t) = \sin(x - 1.57t) + \sin(2x - 3.14t) \tag{3.16}$$

It is seen in Fig. 3.3 that there is no distortion of the waveform.

3.2.2 Dispersion curve

From the discussion above, the phase velocity of a dispersive wave is a function of frequency. The plot of phase velocity versus frequency is a dispersion curve. The dispersion curve of the string wave described in the previous section is shown in Fig. 3.4 using the following parameters

$$T = 1.0 \times 10^5 \, Pa \,, \quad \rho = 1.0 kg / m^3 \,, \quad \mu = 100 N / m^3$$

One important implication from Fig. 3.4 is that there is an asymptotic limit to the frequency, which is $62.8Hz$ on the plot. This limit can be easily derived from Eq. (3.13). In the equation, if $\frac{\omega^2}{c_0^2} - \frac{\mu}{T}$ is less than or equal to zero, the wave number is either a purely imaginary number or zero.

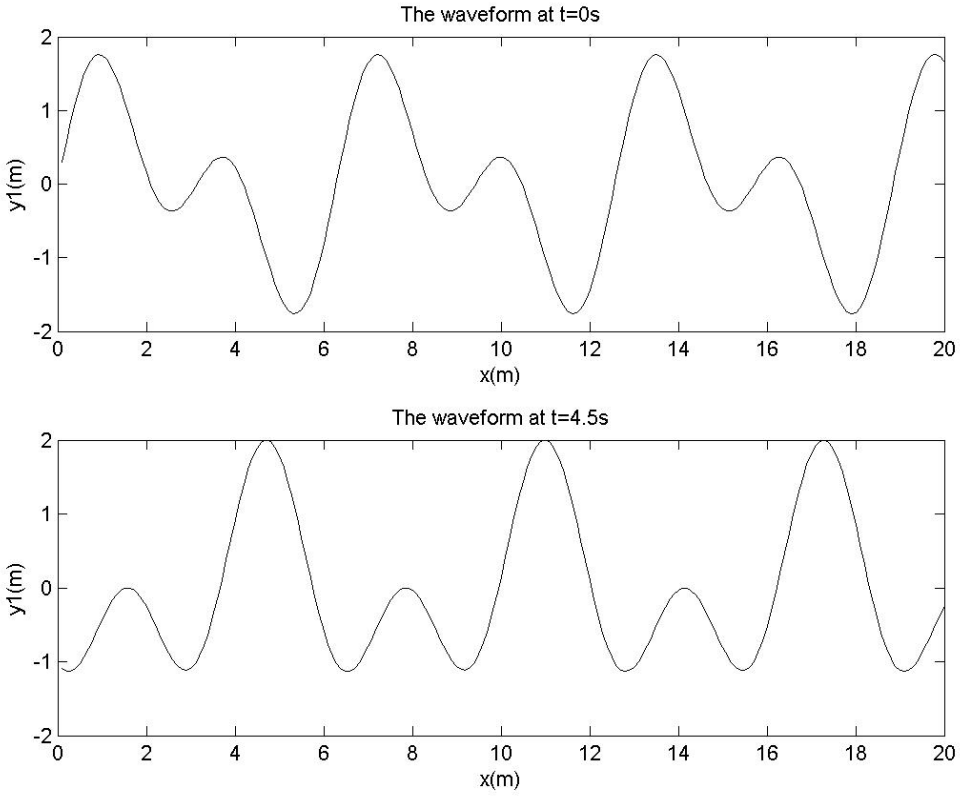

Fig. 3.2 Distortion of dispersive wave

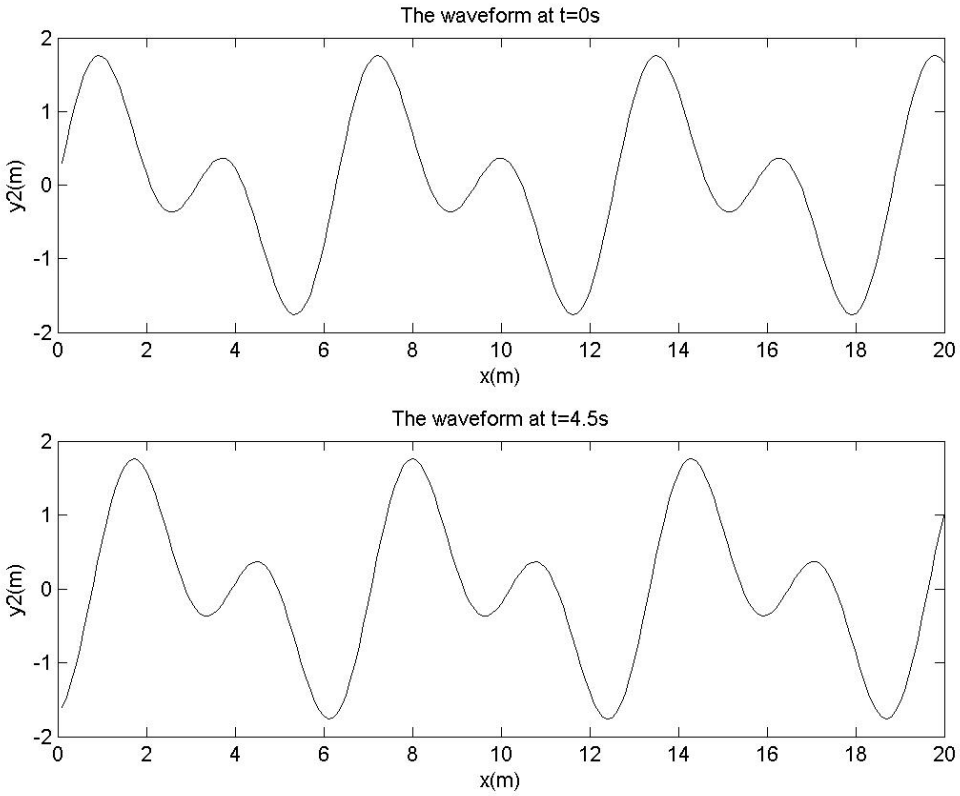

Fig. 3.3 Non-dispersive waves without distortion

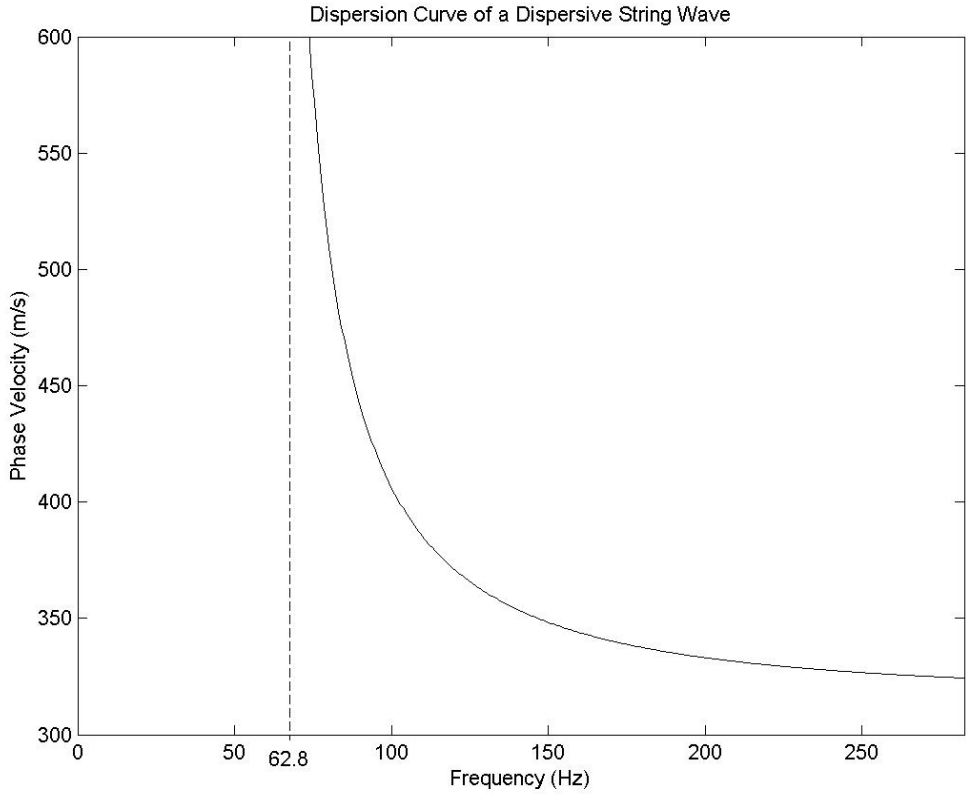

Fig. 3.4 Dispersion curve of a dispersive string wave

This corresponds to a scenario when there is no wave propagation. Therefore there is a limit frequency below which no dispersive waves would propagate. This limit frequency is called the cut-off frequency. The existence of a cut-off frequency is one characteristic that sets the dispersive waves apart from simple harmonic waves.

Another important concept of dispersive waves is the group velocity. As mentioned before, $c_p = \frac{\omega}{k}$ is a phase velocity. Yet another velocity can be defined as $c_g = \frac{d\omega}{dk}$. In the case of nondispersive waves, the corresponding wave velocity is not a function of frequency, thus $c_p = c_g = c$. For dispersive waves, however, these velocities are not equal and each carries a physical interpretation of its own.

3.2.3 Elasto-viscoplastic Lamb waves in plates

Lamb waves are dispersive waves propagating in thin structures with free boundaries. The classic Lamb wave example is a plane wave propagating in an elastic plate structure that satisfies the plane strain condition. Lamb waves occur only when the plate is thin enough so that the plate thickness is comparable with the wavelength.

Lamb waves can propagate in the configuration shown in Fig. 3.5. The associated boundary conditions corresponding to the free surfaces are

$$\sigma_{13} = \sigma_{23} = \sigma_{33} = 0 \text{ , at } x_3 = \pm d \tag{3.17}$$

Under these conditions, the Rayleigh-Lamb characteristic equation for Lamb wave can be derived. There are two different modes of Lamb waves; namely the symmetric modes and the anti-symmetric modes. Their characteristic equations are

$$\frac{\tanh(\beta d)}{\tanh(\alpha d)} = \left(\frac{4k^2 \alpha\beta}{(k^2 + \beta^2)^2} \right)^{\pm 1} \tag{3.18}$$

In (3.18), $\alpha = \sqrt{k^2 - \frac{\omega^2}{c_l^2}}$, $\beta = \sqrt{k^2 - \frac{\omega^2}{c_t^2}}$, c_l and c_t are, respectively, the longitudinal and transverse wave velocity in the media, and $c_l = \sqrt{\frac{\lambda+2\mu}{\rho}}$ and $c_t = \sqrt{\frac{\mu}{\rho}}$, with λ and μ being the Lame constants.

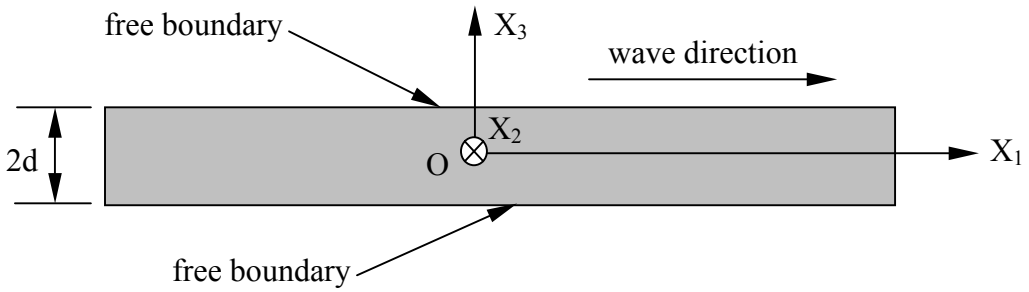

Fig. 3.5 Plate structure that supports Lamb wave propagation

Note that the positive exponent in Eq. (3.18) is for the symmetric modes and the negative sign is for the anti-symmetric modes.

The dispersion curve of a Lamb wave can be obtained from Eq. (3.18). Obviously the dispersion curve is determined by the Lame constants, as well as the thickness of the plate. Since Lame constants are functions of temperature, dispersion curves shift as temperature or plate thickness changes. Therefore shifting of dispersion curve is a good indication of temperature or thickness variations. This is the rational behind the nondestructive evaluation of plates for temperature and thickness measurements. The most commonly used Lamb modes are the first anti-symmetric mode A_0 and the first symmetric mode S_0 because they can be readily observed in experiments. A typical Lamb wave is shown in Fig. 3.6 with both the A_0 and S_0 mode being present. Note that U_3 is the out-of-plane displacement along the x_3-direction.

The dispersion nature of Lamb waves is rooted in the configuration of the elastic media. As stated, wave dispersion occurs when plate thickness and the wavelength are

comparable. Lamb wave dispersion in silicon wafers at elevated temperature is a result of wafer geometry and the elasto-viscoplastic behavior of the material. Due to the complexity of the elasto-viscoplastic constitutive law, a simple characteristic equation similar to Eq. (3.18) cannot be analytically derived. As such, an algorithm must be developed to extract dispersion information from Lamb wave signals. The algorithm will be introduced in Chapter IV. Since both the elastic constants and the plastic constants are functions of temperature, the dispersion curve of the elasto-viscoplastic Lamb waves varies as temperature changes.

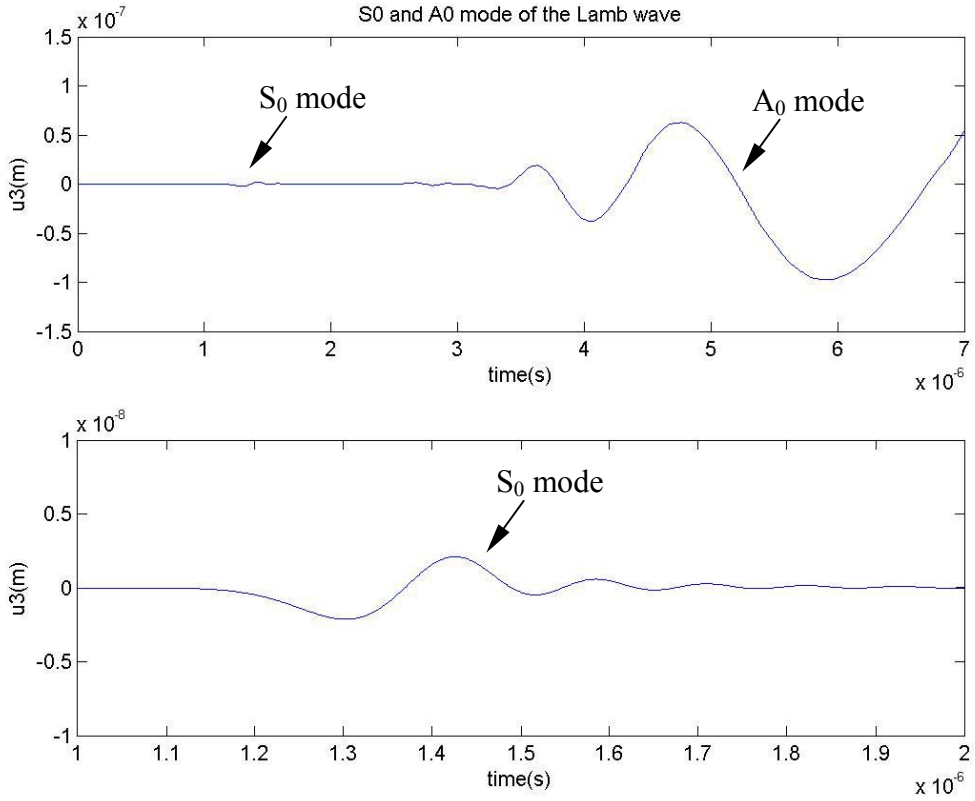

Fig. 3.6 Typical S_0 and A_0 mode of the Lamb wave

3.3 Summary

Stress wave attenuation in silicon wafers is a function of the wafer geometry and material property. Wave excited by a spot source attenuates due to the continuously increasing wavefront. Meanwhile the plastic deformation also dissipates energy. Waves propagating in plastic media attenuate due to the loss of energy to the plastic deformation. Therefore, the parameter for quantifying attenuation must include the influences of both geometry and material property. This idea inspired the definition of attenuation for the single-frequency signals. To define the attenuation of a nonstationary and multi-component wave, the wave must first be decomposed into single frequency components. The process was thoroughly described in this chapter. Stress wave dispersion is also caused by material geometry and property. Dispersive Lamb guided waves can only propagate when the plate thickness is comparable to its wavelength. Since the dispersion curve of a Lamb wave is sensitive to both thickness and material property, which, in turn, are functions of temperature, the dispersion curve of a Lamb wave is a good indicator for thickness and temperature variations. This is the underlying principle of LISWT.

CHAPTER IV

NUMERICAL SOLUTIONS AND EXTRACTION OF FEATURE INFORMATION

In this chapter, a computational model is developed for investigating silicon wafers in response to annealing temperatures beyond 600ºC. Tools needed for the investigation including the staggered-grid finite difference scheme, Gabor wavelet transform and dispersion curve extraction method are also identified. The explicit staggered-grid finite difference scheme is selected to solve the governing equation of the elasto-viscoplastic model presented in Chapter II. Numerical waveforms acquired at two locations that are away from the point of excitation are processed to extract dispersion curves and calculate wave attenuations as functions of temperature and wafer thickness. Since Lamb waves are dispersive, Gabor wavelet transform is employed to find the arrival time of selected frequency components. From the distance of the two sampling locations and the difference between the arrival times, the phase velocity of the selected frequency component can be calculated and the dispersion curve constructed.

4.1 LISWT Computational Model

4.1.1 Model description

The physical configuration considered in the study is a square plate model whose dimensions are given in Fig. 4.1. Note that all dimensions are in mm. Instead of being circular, a square plate model is studied. A general 3D elasto-viscoplastic wave model is developed. If a model were to be developed specifically for circular configuration, due to the geometry and load condition of the problem, an axisymmetric model rather than a general 3D model would be created. This would significantly limit possible future application of the model. Since the model deals with elasto-viscoplastic wave

propagation, it may find applications in other areas other than temperature measurement for semiconductor fabrication. The silicon material model has been described in Chapter II in detail. Since extensive work has been performed by Suh and coworkers [4-8] at temperatures below 600°C, this study focuses on temperatures in the range between 600°C and 1000°C.

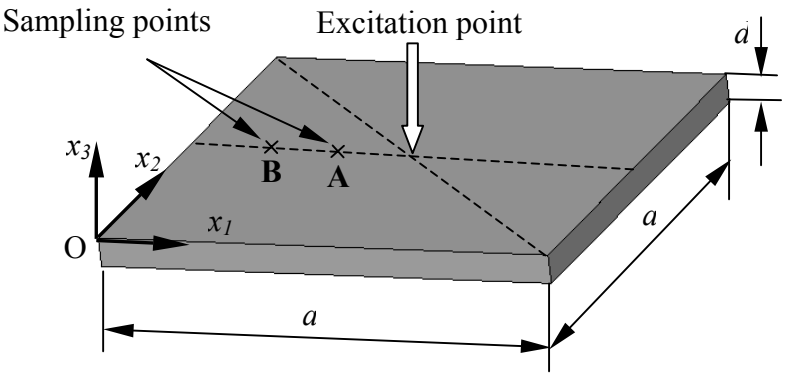

Fig. 4.1 Plate model

4.1.2 Forcing function and initial and boundary conditions

In LISWT, Lamb waves are induced by laser impulse. The excitation of laser-induced stress waves involves a complex, coupled thermal-mechanical process within the volume being heated. It is not the objective of the thesis to study the process. In the investigation, laser excitation is modeled by a stress rate ($Pa/\sec$) with a certain temporal and spatial profile. In the thickness direction, the forcing function is considered constant. Mathematically the input function can be expressed as

$$g(x_1, x_2, t) = F(t)G(x_1, x_2) \tag{4.1}$$

Function $F(t)$ in Eq. (4.1) represents an impulse. Gaussian function is a good approximation for an impulse,

$$F(t) = A\exp[-\frac{(t-\mu)^2}{2\sigma^2}] \tag{4.2}$$

The width of the impulse is controlled by the parameter σ. Note that if $|t-\mu|>3\sigma$ is true, $\exp[-\frac{(t-\mu)^2}{2\sigma^2}]<0.011$. This means the value of $F(t)$ is only 1% of the amplitude A and thus can be ignored. This observation helps to reduce the computational load significantly. The spatial distribution function, $G(x_1,x_2)$, is a two-dimensional Gaussian function. Assume the coordinate of the center of excitation is (X_1,X_2) on the upper surface defined by $x_3 = 0$. The distribution function can be expressed as

$$G(x_1,x_2)=\exp[-\frac{(x_1-X_1)^2+(x_1-X_2)^2}{2\beta^2}] \tag{4.3}$$

The parameter β controls the spot size. Therefore the diameter of the spot is

$$d_s = 6\beta. \tag{4.4}$$

Eq. (4.4) can be used to calculate the parameter β for a particular laser spot size. The time history of the impulse input is shown in Section 4.3 that follows. Fig. 4.2a shows the spatial distribution of the excitation impulse being used for the investigation and Fig. 4.2b gives its size and position in the square plate model. The plate is initially at rest. The initial conditions are that all velocities and stresses are zero at time $t=0$. The boundary conditions are that all four sides of the plates are fixed so that displacements are zero at $x_1=0$, $x_1=a$, $x_2=0$ and $x_2=a$.

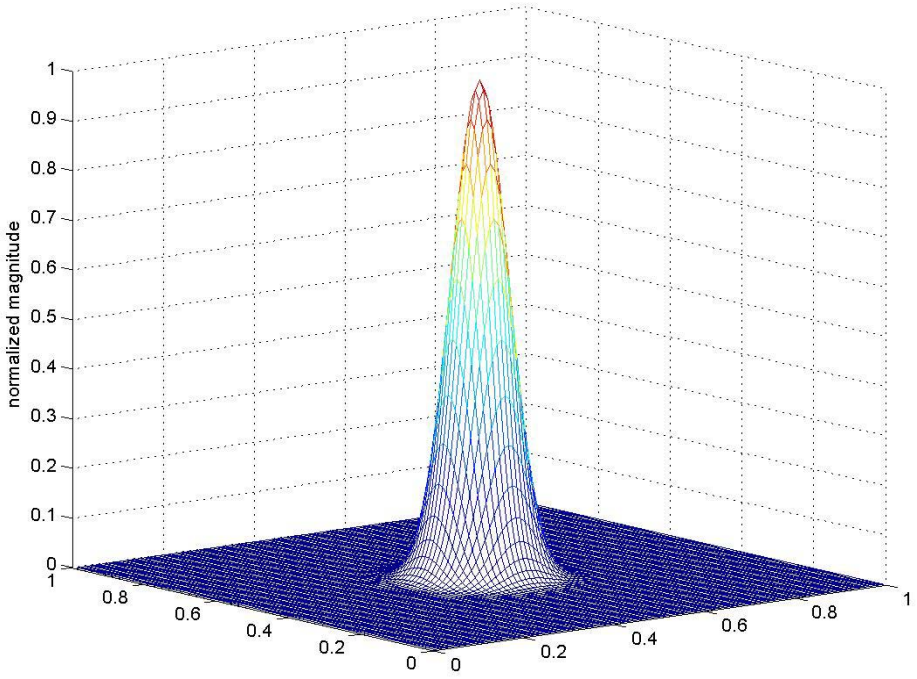

Fig. 4.2a Spatial distribution of excitation

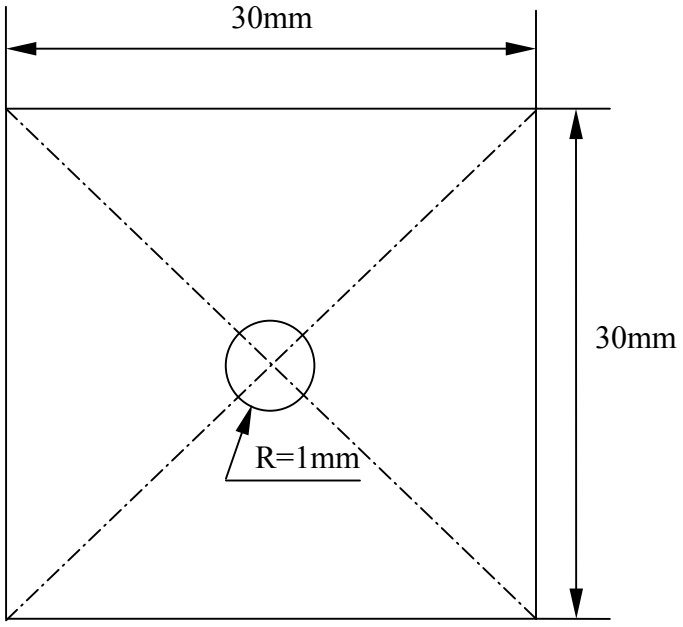

Fig. 4.2b Size and position of the excitation spot (not to scale)

4.2 Staggered-Grid Finite Difference Method

In Chapter II, the governing equation system describing the elasto-viscoplastic wave was derived. It is a first-order hyperbolic equation system of stress and velocity. The physical domain of the problem and initial and boundary conditions were also specified in the previous section. Next the staggered –grid finite difference method is introduced.

There are two methods for the approximation of the first-order derivatives with respect to the spatial coordinates, i.e., the centered grid and the staggered grid. The staggered grid is more accurate than the centered grid. Therefore the staggered gird is widely used to solve wave equations in different disciplines. The word "staggered" means the unknown variables in the equations are not defined on the same grid point. Instead they are halfway off according to their position in the equation. Fig. 4.3 shows the definition of stress and velocity components on one element or control volume in the finite difference mesh. There are explicit and implicit methods for the discretization in the time domain. In the explicit method, there is no need for solving a large-scale linear equation system at each time step, hence less demand on computational load and memory needs. The method is adopted for the study. However, the problem with the explicit scheme is stability. This topic will be discussed, along with the choice of spatial steps, in the next section when numerical examples are presented.

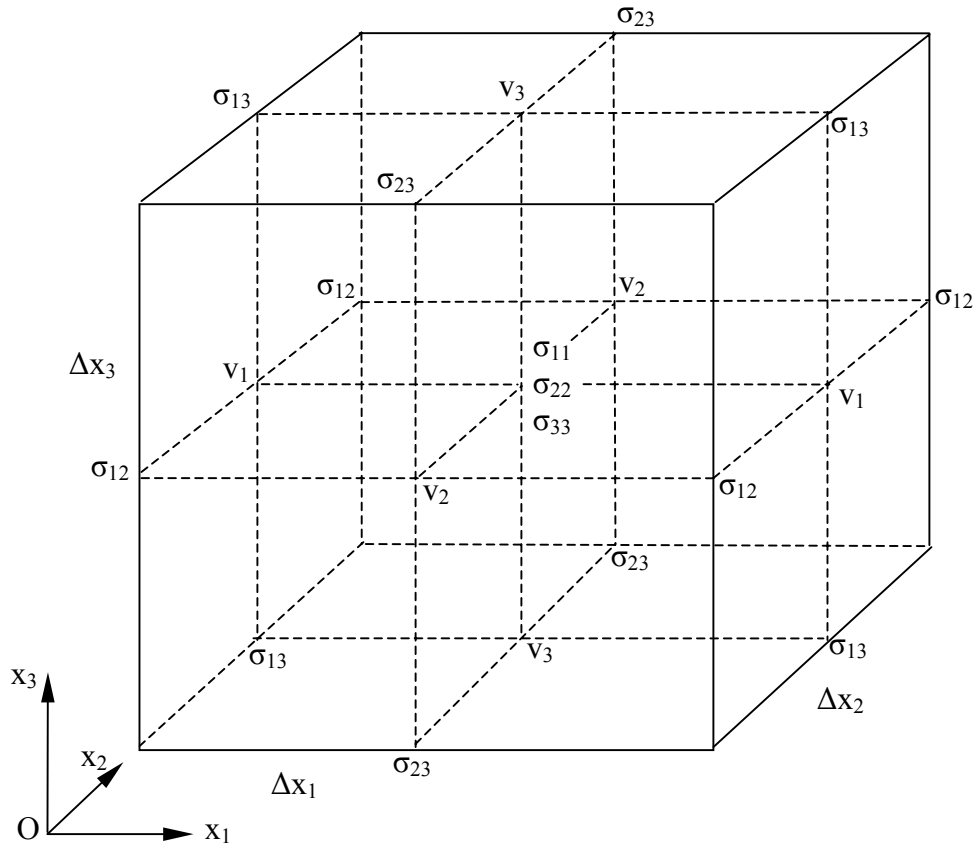

Fig. 4.3 Staggered finite difference scheme

In Fig. 4.3, the normal stresses are defined at the center of the cubic element. The shear stresses are defined at the middle point of the edges. The velocities are defined at the center of the sides. Under this arrangement, stress components are surrounded by velocity components and vice versa, thus defined as the "staggered" scheme. Assume time step, Δt and 3 spatial steps Δx_1, Δx_2 and Δx_3. According to the arrangements in Fig. 4.3, the first-order hyperbolic equation derived in Chapter II can be discretized into the following finite difference equations.

$$\begin{aligned}
&\sigma_{11}^{(n+1)}(i+\frac{1}{2},j+\frac{1}{2},k+\frac{1}{2}) = \sigma_{11}^{(n)}(i+\frac{1}{2},j+\frac{1}{2},k+\frac{1}{2}) \\
&+C_{11}\frac{\Delta t}{\Delta x_1}(v_1^{(n+1/2)}(i+1,j+\frac{1}{2},k+\frac{1}{2}) - v_1^{(n+1/2)}(i,j+\frac{1}{2},k+\frac{1}{2})) \\
&+C_{12}\frac{\Delta t}{\Delta x_2}(v_2^{(n+1/2)}(i+\frac{1}{2},j+1,k+\frac{1}{2}) - v_2^{(n+1/2)}(i+\frac{1}{2},j,k+\frac{1}{2})) \\
&+C_{13}\frac{\Delta t}{\Delta x_3}(v_3^{(n+1/2)}(i+\frac{1}{2},j+\frac{1}{2},k+1) - v_3^{(n+1/2)}(i+\frac{1}{2},j+\frac{1}{2},k)) \\
&-(C_{11}\xi_{11}^{(n)}(i+\frac{1}{2},j+\frac{1}{2},k+\frac{1}{2}) + C_{12}\xi_{22}^{(n)}(i+\frac{1}{2},j+\frac{1}{2},k+\frac{1}{2}) \\
&+C_{13}\xi_{33}^{(n)}(i+\frac{1}{2},j+\frac{1}{2},k+\frac{1}{2}))\Delta t
\end{aligned} \tag{4.5a}$$

$$\begin{aligned}
&\sigma_{22}^{(n+1)}(i+\frac{1}{2},j+\frac{1}{2},k+\frac{1}{2}) = \sigma_{22}^{(n)}(i+\frac{1}{2},j+\frac{1}{2},k+\frac{1}{2}) \\
&+C_{21}\frac{\Delta t}{\Delta x_1}(v_1^{(n+1/2)}(i+1,j+\frac{1}{2},k+\frac{1}{2}) - v_1^{(n+1/2)}(i,j+\frac{1}{2},k+\frac{1}{2})) \\
&+C_{22}\frac{\Delta t}{\Delta x_2}(v_2^{(n+1/2)}(i+\frac{1}{2},j+1,k+\frac{1}{2}) - v_2^{(n+1/2)}(i+\frac{1}{2},j,k+\frac{1}{2})) \\
&+C_{23}\frac{\Delta t}{\Delta x_3}(v_3^{(n+1/2)}(i+\frac{1}{2},j+\frac{1}{2},k+1) - v_3^{(n+1/2)}(i+\frac{1}{2},j+\frac{1}{2},k)) \\
&-(C_{21}\xi_{11}^{(n)}(i+\frac{1}{2},j+\frac{1}{2},k+\frac{1}{2}) + C_{22}\xi_{22}^{(n)}(i+\frac{1}{2},j+\frac{1}{2},k+\frac{1}{2}) + \\
&C_{23}\xi_{33}^{(n)}(i+\frac{1}{2},j+\frac{1}{2},k+\frac{1}{2}))\Delta t
\end{aligned} \tag{4.5b}$$

$$\begin{aligned}
&\sigma_{33}^{(n+1)}(i+\frac{1}{2},j+\frac{1}{2},k+\frac{1}{2}) = \sigma_{33}^{(n)}(i+\frac{1}{2},j+\frac{1}{2},k+\frac{1}{2}) \\
&+C_{31}\frac{\Delta t}{\Delta x_1}(v_1^{(n+1/2)}(i+1,j+\frac{1}{2},k+\frac{1}{2}) - v_1^{(n+1/2)}(i,j+\frac{1}{2},k+\frac{1}{2})) \\
&+C_{32}\frac{\Delta t}{\Delta x_2}(v_2^{(n+1/2)}(i+\frac{1}{2},j+1,k+\frac{1}{2}) - v_2^{(n+1/2)}(i+\frac{1}{2},j,k+\frac{1}{2})) \\
&+C_{33}\frac{\Delta t}{\Delta x_3}(v_3^{(n+1/2)}(i+\frac{1}{2},j+\frac{1}{2},k+1) - v_3^{(n+1/2)}(i+\frac{1}{2},j+\frac{1}{2},k)) \\
&-(C_{31}\xi_{11}^{(n)}(i+\frac{1}{2},j+\frac{1}{2},k+\frac{1}{2}) + C_{32}\xi_{22}^{(n)}(i+\frac{1}{2},j+\frac{1}{2},k+\frac{1}{2}) \\
&+C_{33}\xi_{33}^{(n)}(i+\frac{1}{2},j+\frac{1}{2},k+\frac{1}{2}))\Delta t
\end{aligned} \tag{4.5c}$$

$$\begin{aligned}
&\sigma_{23}^{(n+1)}(i+\frac{1}{2},j,k) = \sigma_{23}^{(n)}(i+\frac{1}{2},j,k) \\
&+\frac{C_{44}}{2}\frac{\Delta t}{\Delta x_3}(v_2^{(n+1/2)}(i+\frac{1}{2},j,k+\frac{1}{2}) - v_2^{(n+1/2)}(i+\frac{1}{2},j,k-1)) \\
&+\frac{C_{44}}{2}\frac{\Delta t}{\Delta x_2}(v_3^{(n+1/2)}(i+\frac{1}{2},j+\frac{1}{2},k) - v_3^{(n+1/2)}(i+\frac{1}{2},j-\frac{1}{2},k)) \\
&-C_{44}\xi_{23}^{(n)}(i+\frac{1}{2},j,k)\Delta t
\end{aligned} \tag{4.5d}$$

$$\begin{aligned}
&\sigma_{13}^{(n+1)}(i,j+\frac{1}{2},k) = \sigma_{13}^{(n)}(i,j+\frac{1}{2},k) \\
&+\frac{C_{55}}{2}\frac{\Delta t}{\Delta x_3}(v_1^{(n+1/2)}(i,j+\frac{1}{2},k+\frac{1}{2}) - v_1^{(n+1/2)}(i,j-\frac{1}{2},k+\frac{1}{2})) \\
&+\frac{C_{55}}{2}\frac{\Delta t}{\Delta x_1}(v_3^{(n+1/2)}(i+\frac{1}{2},j+\frac{1}{2},k) - v_3^{(n+1/2)}(i-\frac{1}{2},j+\frac{1}{2},k)) \\
&-C_{55}\xi_{13}^{(n)}(i,j+\frac{1}{2},k)\Delta t
\end{aligned} \tag{4.5e}$$

$$\begin{aligned}
&\sigma_{12}^{(n+1)}(i,j,k+\frac{1}{2}) = \sigma_{12}^{(n)}(i,j,k+\frac{1}{2}) \\
&+\frac{C_{66}}{2}\frac{\Delta t}{\Delta x_2}(v_1^{(n+1/2)}(i,j+\frac{1}{2},k+\frac{1}{2}) - v_1^{(n+1/2)}(i,j-\frac{1}{2},k+\frac{1}{2})) \\
&+\frac{C_{66}}{2}\frac{\Delta t}{\Delta x_1}(v_2^{(n+1/2)}(i+\frac{1}{2},j,k+\frac{1}{2}) - v_2^{(n+1/2)}(i-\frac{1}{2},j,k+\frac{1}{2})) \\
&-C_{66}\xi_{12}^{(n)}(i,j,k+\frac{1}{2})\Delta t
\end{aligned} \tag{4.5f}$$

$$\begin{aligned}
&v_1^{(n+1/2)}(i,j+\frac{1}{2},k+\frac{1}{2}) = v_1^{(n-1/2)}(i,j+\frac{1}{2},k+\frac{1}{2}) \\
&+\frac{\Delta t}{\rho\Delta x_1}(\sigma_{11}^{(n)}(i+\frac{1}{2},j+\frac{1}{2},k+\frac{1}{2}) - \sigma_{11}^{(n)}(i-\frac{1}{2},j+\frac{1}{2},k+\frac{1}{2})) \\
&+\frac{\Delta t}{\rho\Delta x_2}(\sigma_{12}^{(n)}(i,j+1,k+\frac{1}{2}) - \sigma_{12}^{(n)}(i,j,k+\frac{1}{2})) \\
&+\frac{\Delta t}{\rho\Delta x_3}(\sigma_{13}^{(n)}(i,j+\frac{1}{2},k+1) - \sigma_{13}^{(n)}(i,j+\frac{1}{2},k))
\end{aligned} \tag{4.5g}$$

$$\begin{aligned}
&v_2^{(n+1/2)}(i+\frac{1}{2},j,k+\frac{1}{2}) = v_2^{(n-1/2)}(i+\frac{1}{2},j,k+\frac{1}{2}) \\
&+\frac{\Delta t}{\rho\Delta x_1}(\sigma_{12}^{(n)}(i+1,j,k+\frac{1}{2}) - \sigma_{12}^{(n)}(i,j,k+\frac{1}{2})) \\
&+\frac{\Delta t}{\rho\Delta x_2}(\sigma_{22}^{(n)}(i+\frac{1}{2},j+\frac{1}{2},k+\frac{1}{2}) - \sigma_{22}^{(n)}(i+\frac{1}{2},j-\frac{1}{2},k+\frac{1}{2})) \\
&+\frac{\Delta t}{\rho\Delta x_3}(\sigma_{32}^{(n)}(i+\frac{1}{2},j,k+1) - \sigma_{32}^{(n)}(i+\frac{1}{2},j,k))
\end{aligned} \tag{4.5h}$$

$$
\begin{aligned}
&v_3^{(n+1/2)}(i+\frac{1}{2},j,k+\frac{1}{2}) = v_3^{(n-1/2)}(i+\frac{1}{2},j,k+\frac{1}{2}) \\
&+\frac{\Delta t}{\rho \Delta x_1}(\sigma_{13}^{(n)}(i+1,j+\frac{1}{2},k)-\sigma_{13}^{(n)}(i,j+\frac{1}{2},k)) \\
&+\frac{\Delta t}{\rho \Delta x_2}(\sigma_{23}^{(n)}(i+\frac{1}{2},j+1,k)-\sigma_{23}^{(n)}(i+\frac{1}{2},j,k)) \\
&+\frac{\Delta t}{\rho \Delta x_3}(\sigma_{33}^{n}(i+\frac{1}{2},j+\frac{1}{2},k+\frac{1}{2})-\sigma_{33}^{n}(i+\frac{1}{2},j+\frac{1}{2},k-\frac{1}{2}))
\end{aligned}
\tag{4.5i}
$$

In Eq. (4.5), the superscript is the time step index. The "$\frac{1}{2}$" in the index indicates the "staggered" arrangements. In Eqs. (4.7a)-(4.7f), $\xi_{ij}^{(n)}$ is the plastic strain rate. According to the plastic constitutive law described in Chapter II,

$$\xi_{ij}^{(n)}(i,j,k) = f^{(n)}\,\bar{\sigma}_{ij}^{(n)}(i,j,k), \tag{4.6}$$

where f was defined in Chapter II and $\bar{\sigma}_{ij}$ is the deviatoric stress.

Successful extension of the staggered grid scheme from the elastic zone into the plastic zone lies in the fact that each component of deviatoric stress tensor and the corresponding component of the stress tensor can be defined on the same grid point. For example, according to this staggered scheme, $\bar{\sigma}_{11} = \sigma_{11} - \frac{1}{3}(\sigma_{11}+\sigma_{22}+\sigma_{33})$ can be legitimately defined at the center of the finite difference element without involving other grid points on the element, as where σ_{11}, σ_{22} and σ_{33} are defined. This insures that the accuracy of the staggered scheme is maintained. In other words, if in Eq. (4.6), $\bar{\sigma}_{11}$, for instance, cannot be legitimately defined at the center of the finite difference element but involves other grid points on the element, as where σ_{11}, σ_{22} and σ_{33} are, then $\xi_{11}^{(n)}(i,j,k)$ is not defined strictly at the center. Rather, it involves other grid points on the element. In this case, the staggered nature of Eq. (4.5a) is no longer preserved because stresses are no longer completely surrounded by velocities.

4.3 Numerical Results

In this section, the problem of choosing appropriate time and spatial steps will be addressed with numerical examples. For the explicit scheme employed in the investigation, a small enough time step must be found to ensure solution convergence. However, an excessively small time step will unnecessarily add to the computational load. The criterion for stability, or the Courant Condition, is

$$\Delta t \le \frac{1}{c_{\max}\sqrt{\frac{1}{\Delta x_1^2}+\frac{1}{\Delta x_2^2}+\frac{1}{\Delta x_3^2}}} \tag{4.7}$$

Usually the maximum wave velocity in the medium is the longitudinal wave velocity. Therefore in Eq. (4.7), $c_{\max} = c_l = \sqrt{\frac{\lambda + 2\mu}{\rho}}$, with λ and μ being the Lame constants and ρ the mass density of the medium. This condition states that the time step must be less than the time the propagating wave takes to travel across one element in the finite difference scheme.

The selection of proper spatial steps is also presented here. As mentioned before, large spatial steps may cause numerical dispersion and compromise the accuracy of results. In addition, larger spatial steps necessitates small time step. The best way to find the right spatial steps is to carry out numerical experiments on the specific problem at hand. The problem involves the silicon plate shown in Fig. 4.1 whose dimension is $30mm * 30mm * 0.5mm$. Since the temperature range is from 600°C to 1000°C, the waveforms for 600°C and 1000°C are studied.

The duration of the impulse input is 10 nanoseconds and its time profile is shown in Fig. 4.4. To meet the stability requirement, a small time step, $\Delta t = 5 \times 10^{-10} s$, is chosen for the time being. Waveforms acquired at Point B, which is 10-mm from the excitation point are studied. Four cases with different mesh sizes are considered. Table 4.1 shows the mesh sizes.

Results for 600°C and 1000°C are presented in Figs. 4.5a and 4.5b, respectively. The S_0 mode and the A_0 mode can be clearly identified. Also it can be seen that the data is converging. Since there is little difference between mesh size CASE 3 and CASE4, 300mm*300mm*5mm is chosen for the study. The corresponding element size is 0.1mm*0.1mm*0.1mm. With the mesh and element sizes, the maximum allowed time step can be calculated according to the condition $\Delta t \leq 7.194 \times 10^{-9} s$.

When temperature increases, wave velocity decreases so the limit on the time step is relaxed. This condition provides an upper limit on the time step for stability but not necessarily for accuracy. To ensure accuracy, usually a much smaller time step is preferred. The time step chosen for the investigation is 1ns, which is almost an order of magnitude smaller than is required by the stability criterion.

Table 4.1

Mesh sizes

CASE 1	100mm*100mm*5mm
CASE 2	150mm*150mm*5mm
CASE 3	200mm*200mm*5mm
CASE 4	300mm*300mm*5mm

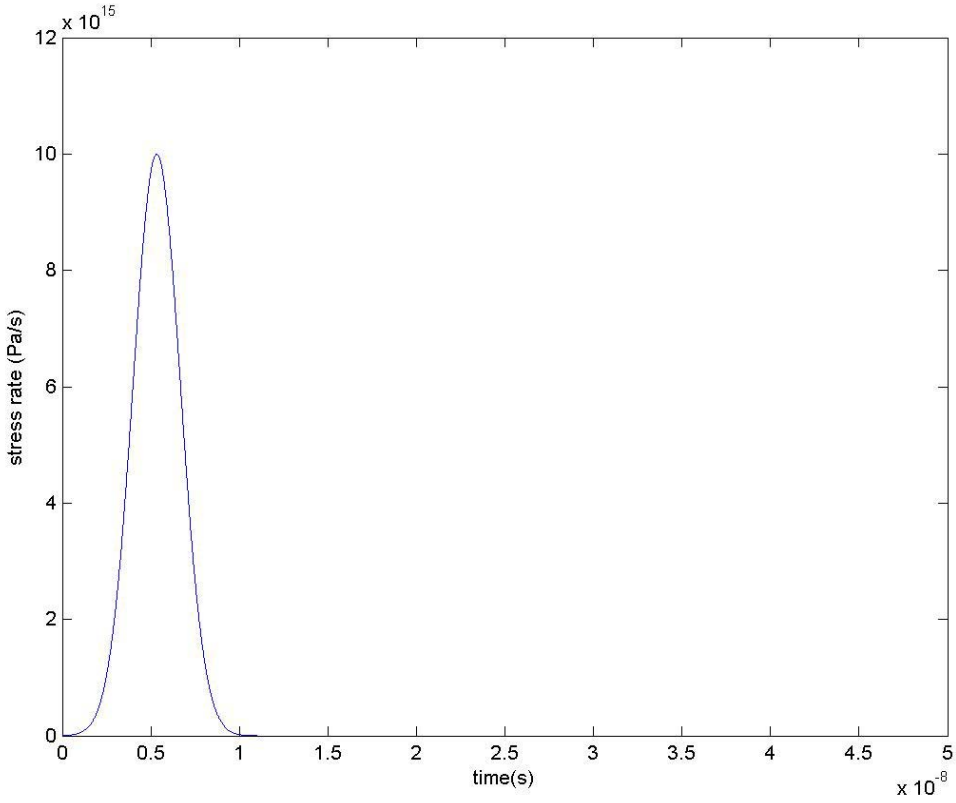

Fig. 4.4 Excitation impulse

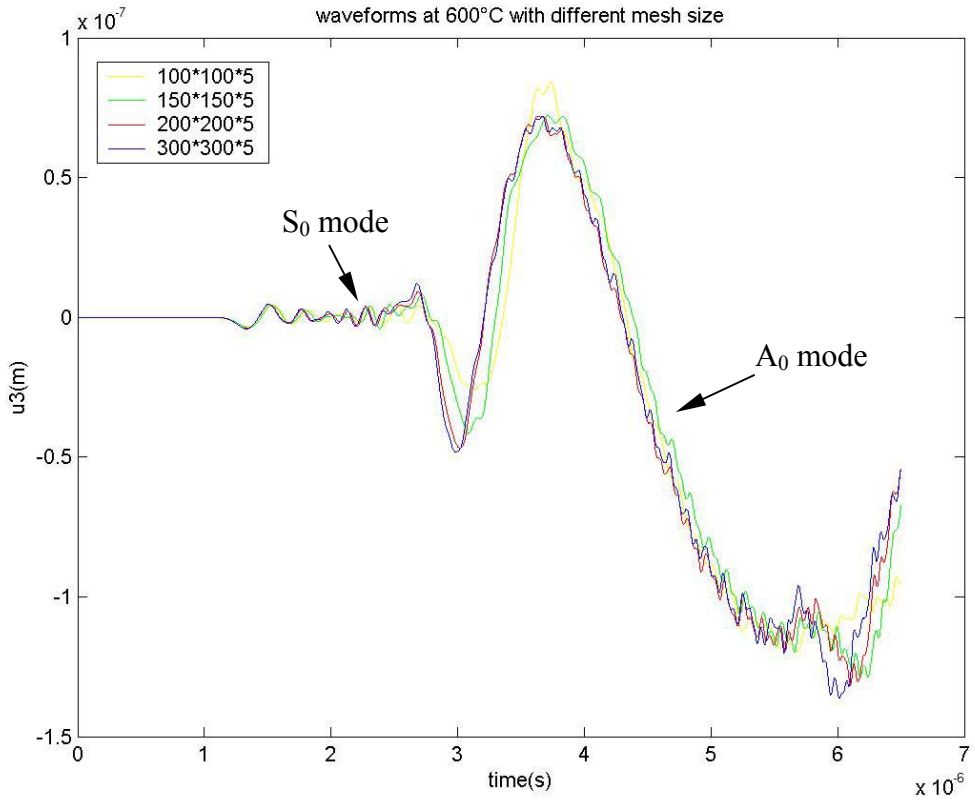

Fig. 4.5a Waveforms acquired at point B at 600°C with different mesh sizes

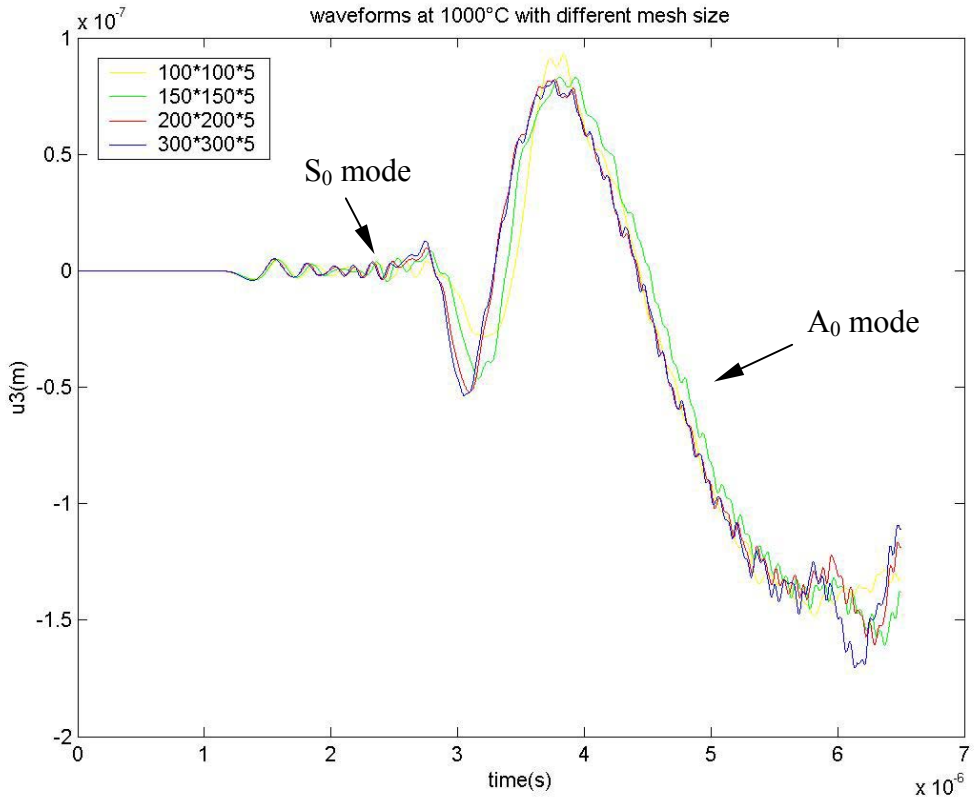

Fig. 4.5b Waveforms acquired at point B at 1000°C with different mesh sizes

4.4 Gabor Wavelet Transform

4.4.1 Signal processing tools

To identify the frequency characteristics of the signals obtained from experiments or simulations, an appropriate signal processing tool must be found. Fourier Transform (FT) has long been a widely used tool. The basic idea of Fourier Transform is to use a set of sinusoidal functions with different frequencies as the bases and decompose the signal into a weighted sum of the bases. The following is the Fourier transform of $x(t)$,

$$X(\omega) = \int_{-\infty}^{\infty} x(t) e^{-j\varpi t} dt \tag{4.8}$$

Discrete Time Fourier Transform (DTFT) is an algorithm applicable to process real-world discrete time sequences. The definitions of DTFT are

$$X[k] = \sum_{n=0}^{N-1} (x[n] e^{-j2\pi nk/M}), k = 0,1,2...M-1 \tag{4.9}$$

where N is the number of points in the time sequence and M is the number of points in the frequency domain with $M \geq N$. A larger M will give better visual representations though it does not really change the resolution.

Fourier Transform, with its wide range of applications, has its limitations. For example, it cannot be applied to signals whose frequency structure changes with time. Chirp signal is such an example. The problem lies with the fact that Fourier Transform uses a set of sinusoidal functions as the bases and assumes time-invariant spectral components of the signal. The transformed result contains only the frequency information. The implication is that the resulted frequency structure applies to any moment of the signal duration. This is not true for a large category of signals such as the chirp signal. Therefore Fourier Transform is inherently inadequate for analyzing time-varying signals. Short Time Fourier Transform (STFT) is one of the solutions to such a need. Unlike the infinite-support bases that span the Fourier Transform, STFT utilizes a windowed sinusoidal function,

$$X(\omega, \tau) = \int_{-\infty}^{\infty} x(t) \psi(t-\tau) e^{-j\omega t} dt \tag{4.10}$$

where $\psi(t)$ is the window function. It can be seen that, with a short-support window function, the transform in Eq. (4.10) represents the Fourier Transform in the vicinity of time τ. In other words, STFT resolves the spectral information of the signal at time τ. The difference between FT and the STFT is essential. FT is a frequency analysis tool that assumes an invariant frequency structure and is applicable only to stationary signal. STFT, on the other hand, is a time-frequency analysis tool that resolves the spectrum of the signal at different time. Thus STFT is applicable to both stationary and nonstationary signals. The discrete STFT is defined as

$$X[n,k]=\sum_{l=0}^{M-1}x[n+l]\psi[l]e^{-j2\pi lk/N} \tag{4.11}$$

where k is similar to the frequency index in Eq. (4.9) and M is the number of points in the window function. Though a welcome alternative to FT, STFT is not without limitation. In Eq. (4.10), the window function is fixed for all frequencies and times. On the time-frequency plane, the resolution of the analysis is the same at all locations. See Fig. 4.6. For a generic block in Fig. 4.6, Δt is the width of the window function in the time domain and Δω is its width in the frequency domain. t^* and ω^* indicate the time and frequency at which the transform is performed.

All time-frequency analysis tools comply with the uncertainty principle, which states that the time resolution and frequency resolution of the analysis cannot go arbitrarily high at the same time. As shown in Fig. 4.6, for the block on the time-frequency plane, the uncertainty principle gives

$$\Delta\omega * \Delta t \geq 0.5 \tag{4.12}$$

The equality in (4.12) occurs when the window is a Gaussian function. The STFT with a Gaussian window function is called Gabor Transform.

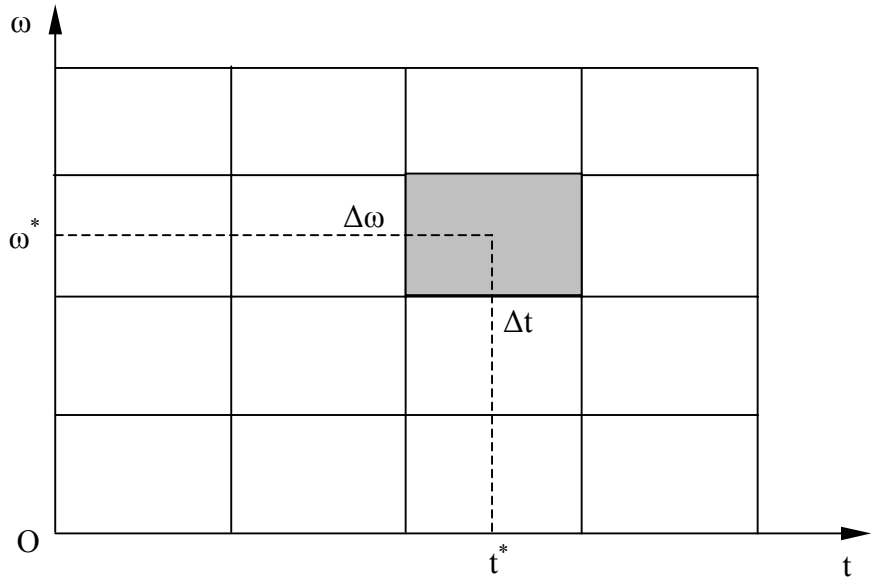

Fig. 4.6 Time-frequency resolution of STFT

4.4.2 Wavelet Transform

As mentioned in the previous section, resolution of STFT is the same everywhere on the time-frequency plane. The disadvantage of this property is obvious. To improve time (frequency) resolution, a short (wide) window is needed. An intuitive way to resolve this dilemma is to have short high frequency windows and wide low frequency windows. This is exactly what the wavelet transform offers.

$$X_w(a,b) = \frac{1}{\sqrt{a}} \int_{-\infty}^{\infty} \bar{\psi}(\frac{t-b}{a}) x(t) dt \tag{4.13}$$

In Eq. (4.13), $\psi(t)$ is the basic wavelet function and $\bar{\psi}(t)$ is it complex conjugate. The basic wavelet function must satisfy the following admissible condition,

$$\int_{-\infty}^{\infty} \frac{|\hat{\psi}(\omega)|^2}{|\omega|} d\omega < \infty, \tag{4.14}$$

where $\hat{\psi}(\omega)$ is the Fourier Transform of $\psi(t)$. A weak condition to make Eq. (4.14) hold is

$$\hat{\psi}(\omega) = 0, \tag{4.15}$$

which is equivalent to

$$\int_{-\infty}^{\infty} \psi(t) dt = 0. \tag{4.16}$$

According to Eq. (4.16), a valid basic wavelet function must have zero-crossings on the time axis, i.e., it exhibits the wave property, thus being called a wavelet function. The parameter b in Eq. (4.13) corresponds to the time on the time-frequency plane. The parameter a indicates frequency content but is not frequency itself. Assume the basic wavelet function $\psi(t)$ is centered at $t = 0$ with a width W and its Fourier Transform $\hat{\psi}(\omega)$ is centered at $\omega = \omega_0$ with a width $\tilde{W}$. Then $\psi(\frac{t-b}{a})$ is centered at $t = b$ and its Fourier transform $a \exp(-ib\omega)\hat{\psi}(a\omega)$ is centered at $\omega = \frac{\omega_0}{a}$. Therefore a particular pair

of (b,a) in the wavelet transform corresponds to an area with a width aW along the time axis and a width $\frac{\tilde{W}}{a}$ along the frequency axis. The area is centered at the point $(b,\frac{\omega_0}{a})$ on the time-frequency plane. From the above discussion, it is easily concluded that the resolution of wavelet transform on the time-frequency plane changes with location as shown in Fig. 4.7. Like all other time-frequency analysis tool, the wavelet transform also follows the uncertainty principle.

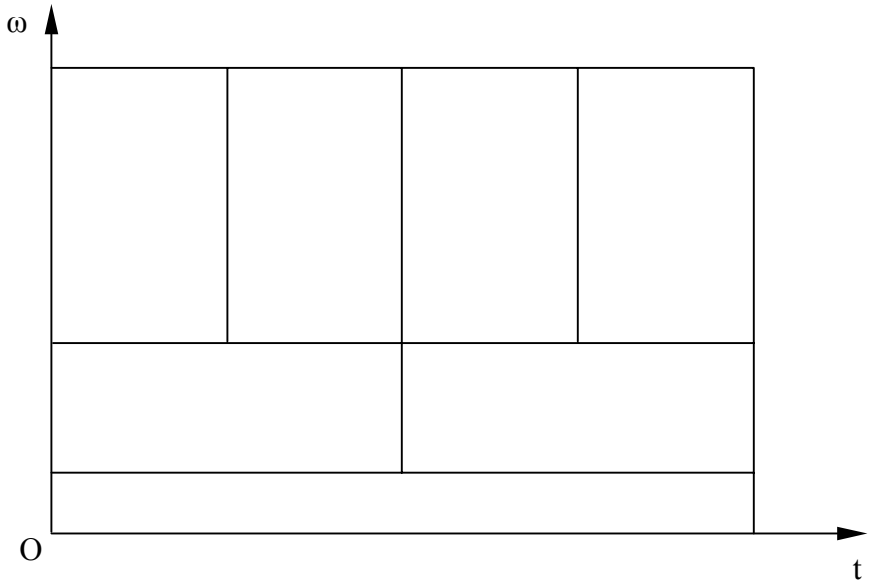

Fig. 4.7 Time-frequency resolution of wavelet transform

4.4.2 Gabor Wavelet Transform

Gabor Wavelet Transform adopts Gabor function as the basic wavelet function which is expressed as

$$\psi_g(t) = \frac{1}{\sqrt[4]{\pi}}\sqrt{\frac{\omega_0}{\gamma}}\exp\left[-\frac{(\omega_0/\gamma)^2}{2}t^2 + i\omega_0 t\right] \tag{4.17}$$

The Fourier Transform of the Gabor function is

$$\hat{\psi}_g(\omega) = \frac{\sqrt{2\pi}}{\sqrt[4]{\pi}} \sqrt{\frac{\gamma}{\omega_0}} \exp\left[-\frac{(\omega_0/\gamma)^2}{2} (\omega - \omega_0)^2 \right] \tag{4.18}$$

From Eq. (4.17), the Gabor function is a sinusoidal function modulated by an exponential function. Since it controls the width of the Gabor function, γ has an impact on the time-frequency resolution. The influence of γ is shown by some examples in the following. When $\omega_0 = 2\pi$ and $\gamma = 3.0$ the function and its Fourier Transform are shown in Figs. 4.8 and 4.9, respectively.

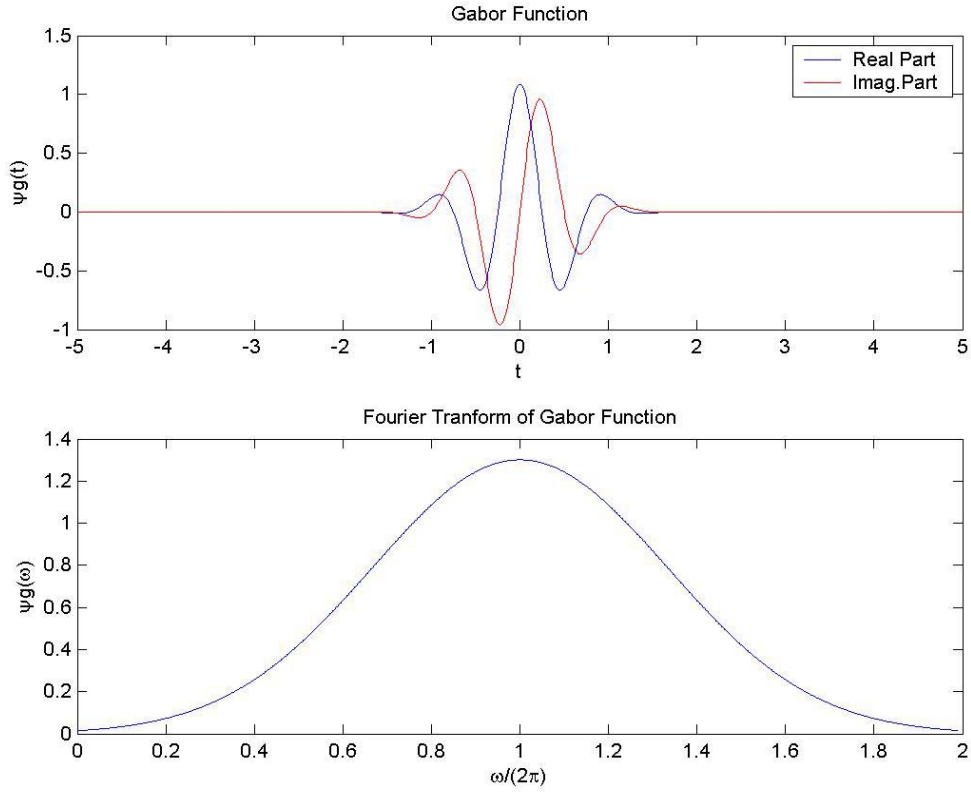

Fig. 4.8 Gabor function and its Fourier Transform

4.4.3 Influence of parameter γ in Gabor Wavelet Transform

As mentioned above, γ influences the time-frequency resolution because it determines the width of the basic Gabor function. Consider the two-component signal in Fig.3.1 in Chapter III. The Gabor Wavelet Transform of the signal with $\gamma = 1.0$, $\gamma = 3.0$ and $\gamma = 6.0$ are given in Figs. 4.9 - 4.11, respectively. In Fig. 4.9, the basic Gabor wavelet function width is the smallest. A narrow wavelet function leads to high resolution in the time domain but low resolution in the frequency domain. From Fig. 4.9 it is clear that signal frequency changes at $t = 6s$. The time resolution is the highest. But the frequency cannot be identified on the plot because it spreads out due to low resolution in frequency.

In Fig. 4.10, the basic Gabor wavelet function width is larger than that in Fig. 4.9. Therefore its time resolution is lower than Fig. 4.9 but its frequency resolution is higher. From Fig. 4.10, the time at which signal frequency changes is not as sharp as that in Fig. 4.9, although it can be said to be around $t = 6s$. The frequency of the signal, however, can be now identified as being centered around $1Hz$ and $3Hz$.

In Fig. 4.11, the basic Gabor wavelet function width is the largest. Therefore its time resolution is the lowest but its frequency resolution is the highest. The time when the signal frequency changes is hard to identify in Fig. 4.10. The frequency of the signal, however, can be clearly identified as $1Hz$ and $3Hz$. As stated by the uncertainty principle, time and frequency resolution cannot be improved simultaneously. When γ increases, frequency resolution increases accordingly but time resolution drops. On the other hand, when γ decreases, frequency resolution drops but time resolution increases. To identify the proper γ value, it is necessary to run a few numerical trials. The γ value experimentally determined for the study is 3.0.

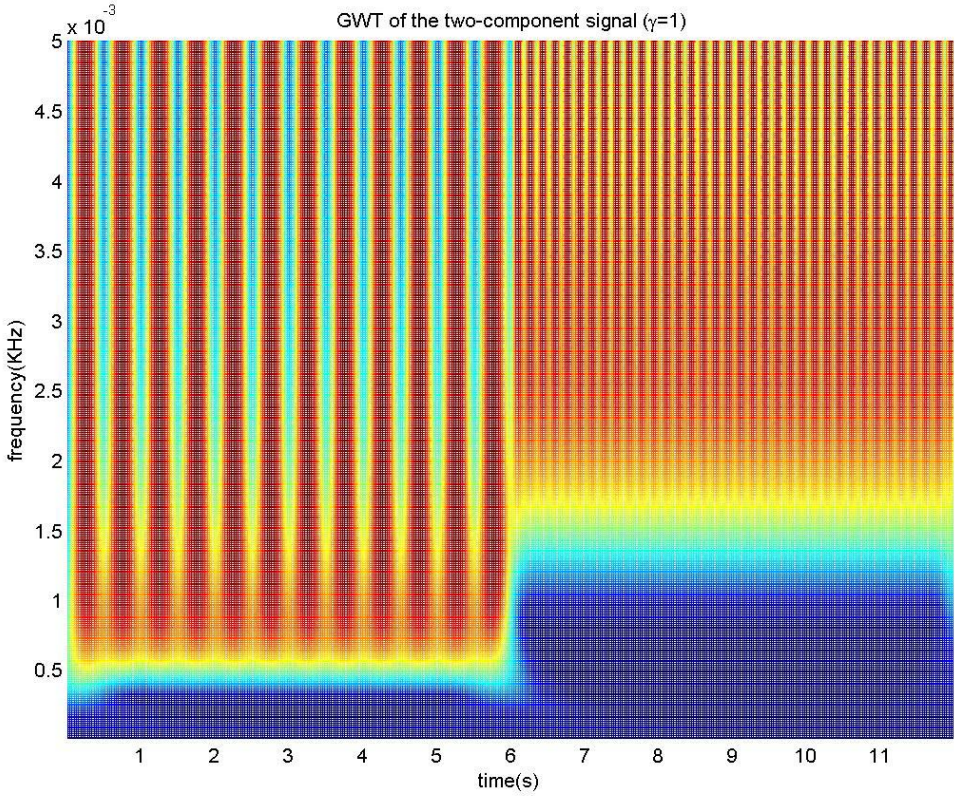

Fig. 4.9 GWT of the two-component signal (γ=1.0)

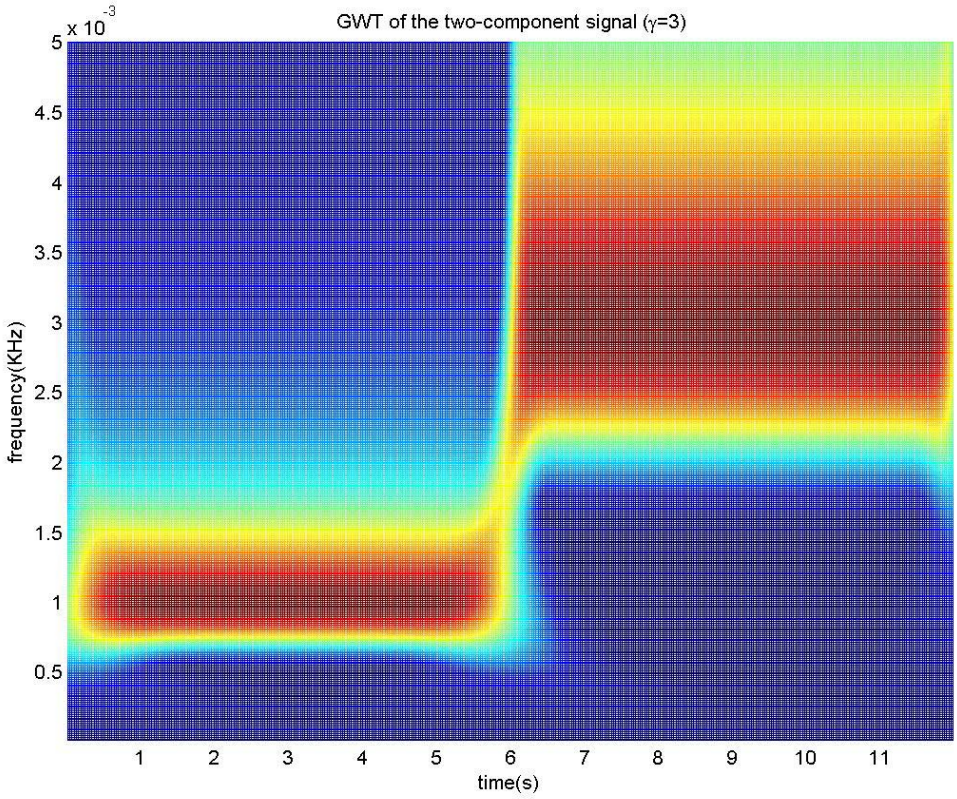

Fig. 4.10 GWT of the two-component signal (γ=3)

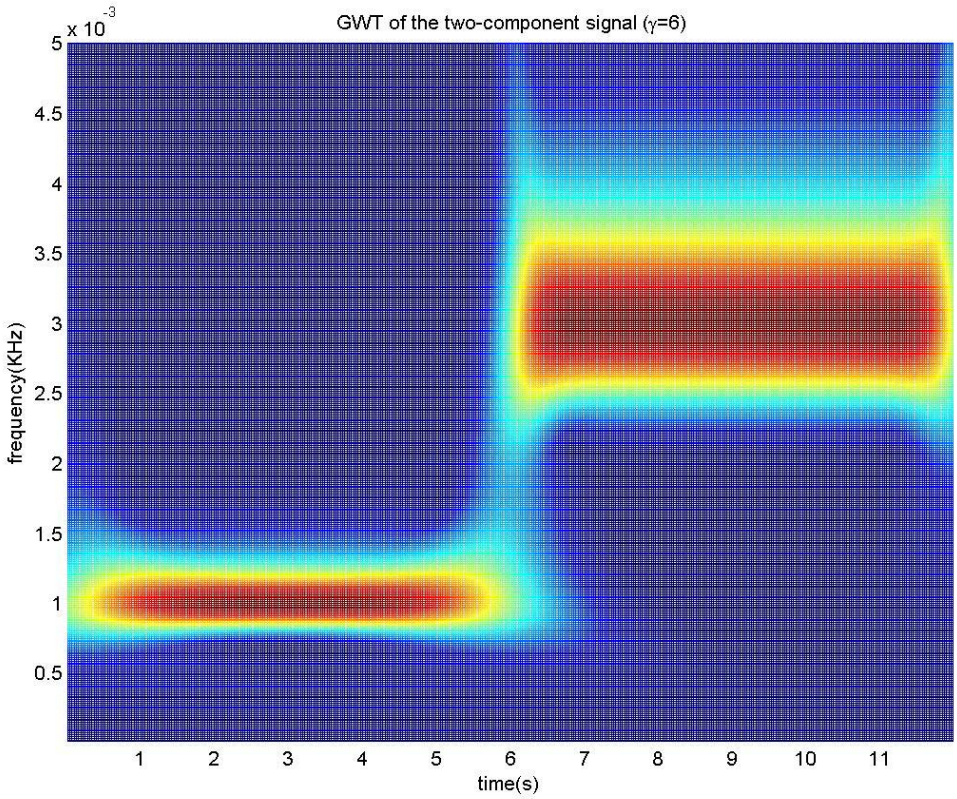

Fig. 4.11 GWT of the two-component signal (γ=6)

4.5 Extraction of Dispersion Curves

As shown in Fig. 4.1, waveforms were acquired from two locations A and B. Assume the distance between these two points is *d*. The GWT is then performed on the acquired waveforms. For a particular frequency component, the time location corresponding to the maximum GWT magnitude indicates the arrival time of the frequency [8]. If the arrival times of the particular frequency component at locations A and B are $t_A(\omega)$ and $t_B(\omega)$, respectively, the travel time for this frequency component over the distance d is

$$\Delta t(\omega) = t_B(\omega) - t_A(\omega) \tag{4.19}$$

Figs. 4.12a and 4.12b show how the arrival time is determined for the signal in Fig. 4.5a with the 300mm*300mm*5mm mesh size at *d* = 10mm and *d* = 5mm.

The phase velocity of the frequency can be determined using

$$v_p(\omega) = \frac{d}{\Delta t(\omega)} \tag{4.20}$$

Eq. (4.20) gives the relation between phase velocity, v_p, and frequency, ω, which then can be plotted as dispersion curves.

4.6 Summary

In this chapter, the numerical scheme and the time-frequency analysis tool were developed. Issues regarding choosing parameters for the explicit staggered grid finite difference scheme and Gabor Wavelet Transform were also discussed. Because the stability of the explicit method depends on the time step, a 1-nanosecond time step was chosen for the study. The time step is smaller than what is required by the Courant Condition to ensure accuracy. Spatial steps were also appropriately chosen to eliminate undesirable numerical dispersion. A trial-and-error procedure was followed to ensure convergence and a 300mm*300mm*5mm mesh size was chosen as a result. The Gabor Wavelet Transform provides the best overall time-frequency resolution. The parameter

γ in the Gabor function has an immediate impact on the time-frequency resolution -- a larger γ means better frequency resolution but poorer time resolution. On the contrary, a smaller γ means better time resolution but poorer frequency resolution. γ was chosen to be 3.0 in the study after extensive numerical experiments. Procedures described in this chapter will be followed in the next chapter to establish the correlation between temperature and thickness with wave attenuation and wave dispersion in silicon wafers.

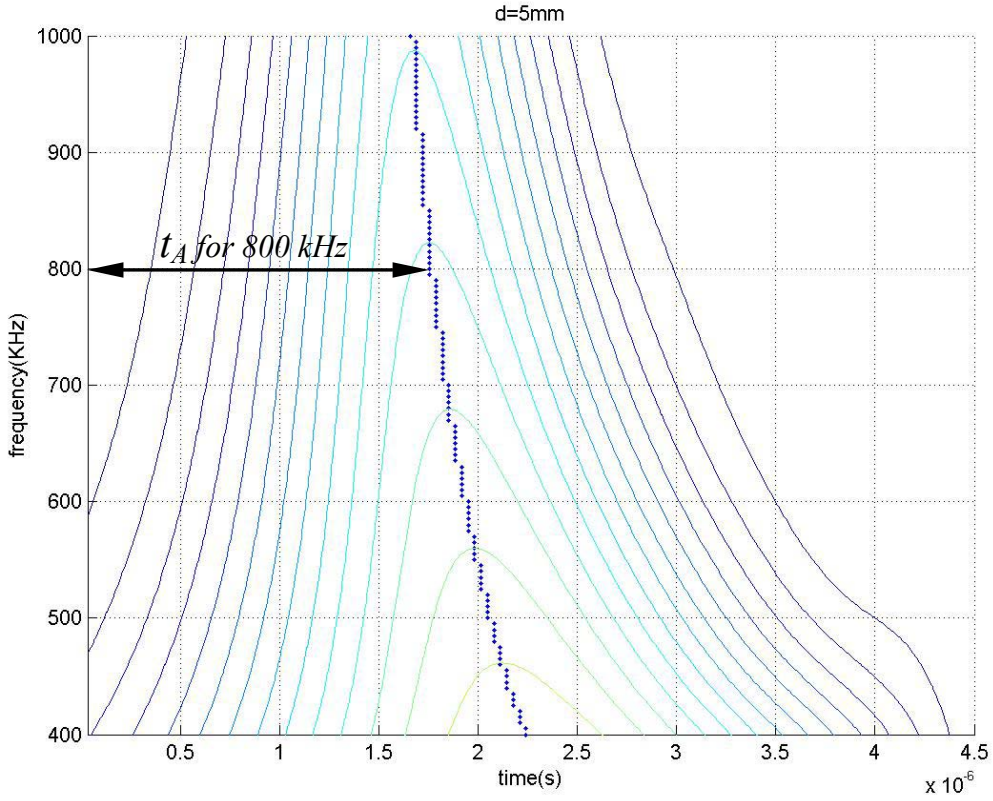

Fig. 4.12a Determination of signal arrival time of 800 kHz component at d =5mm

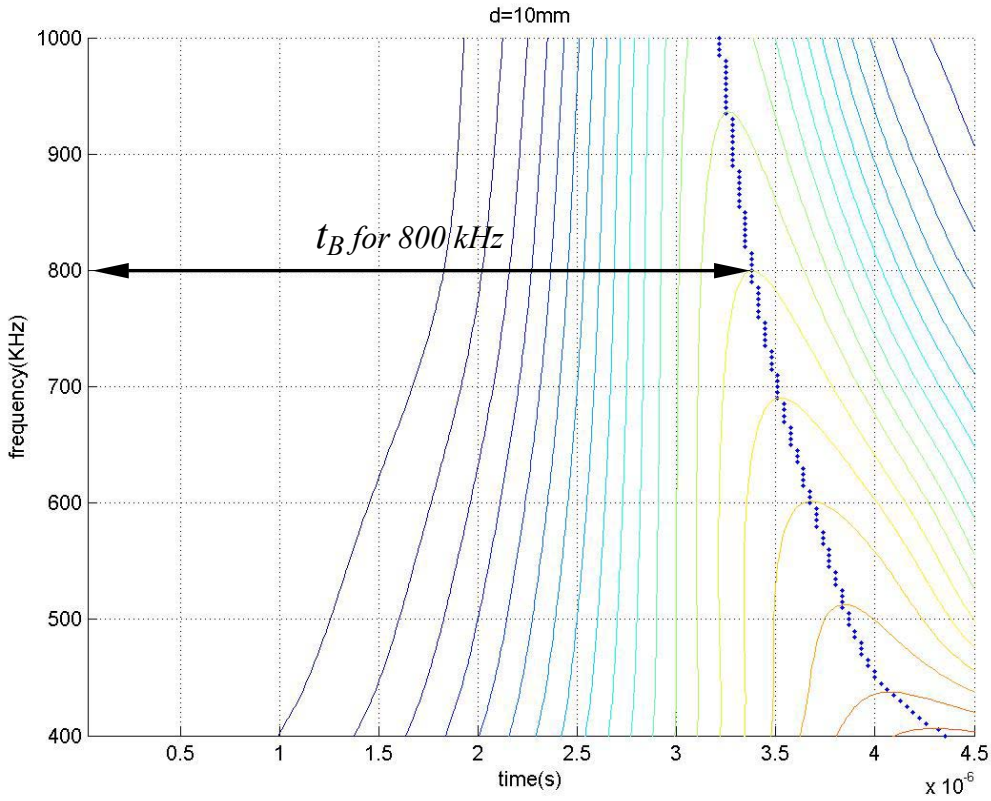

Fig. 4.12b Determination of arrival time of 800 kHz component at d = 10mm

CHAPTER V

WAVE PROPAGATION SUBJECT TO THERMAL AND SPATIAL VARIATIONS

5.1 Temperature Influence on Wave Attenuation

Fig 5.1 plots the attenuation factor, Q, as functions of temperature for three frequency components. Three plate thickness are considered; namely, 0.2mm, 0.35mm and 0.5mm. It is observed from Figs. 5.1a-5.1c that in general the higher the frequency, the more prominent the attenuation factor changes with temperature, thus indicating better temperature resolution. In addition, for all the frequencies considered, the attenuation factor is a nonlinear function of temperature, thus signifying the nonlinearity of the plastic constitutive law. These observations suggest that in order to achieve better temperature resolution using attenuation, high frequency components should be used to resolve temperature higher than 600°C. Fig. 5.2 shows the attenuation factor corresponding to the 800kHz frequency component as a function of temperature for three different plate thicknesses. Table 5.1 summarizes the change of attenuation factor caused by 1°C change of temperature at the same frequency. The table can be used to calibrate temperature resolution within each of the noted temperature range using attenuation.

5.2 Thickness Influence on Wave Attenuation

Attenuation factors as functions of thickness at three different temperatures are shown in Fig. 5.3a through Fig. 5.3c. Again, frequency components 400kHz, 650kHz and 900kHz are considered. It is observed that the higher the frequency, the faster the attenuation factor varies with thickness. For the lowest frequency considered, 400kHz, it is difficult to summarize a general rule of how attenuation factor changes with thickness.

The attenuation factor corresponding to 900kHz frequency is plotted against thickness for three different temperatures in Fig. 5.4. Table 5.2 summarizes the change of attenuation factor caused by 0.1mm change in thickness at the same frequency. The table can be used to calibrate thickness variation at each of the three noted temperature using attenuation.

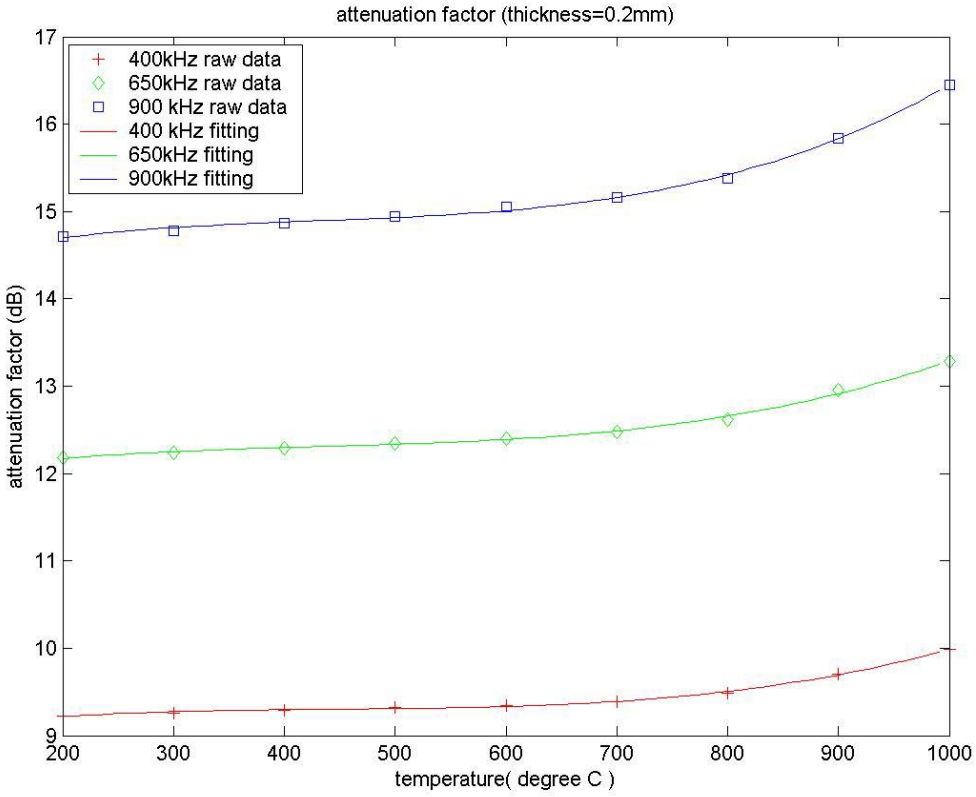

Fig. 5.1a Attenuation factor vs. temperatures for plate thickness=0.2mm

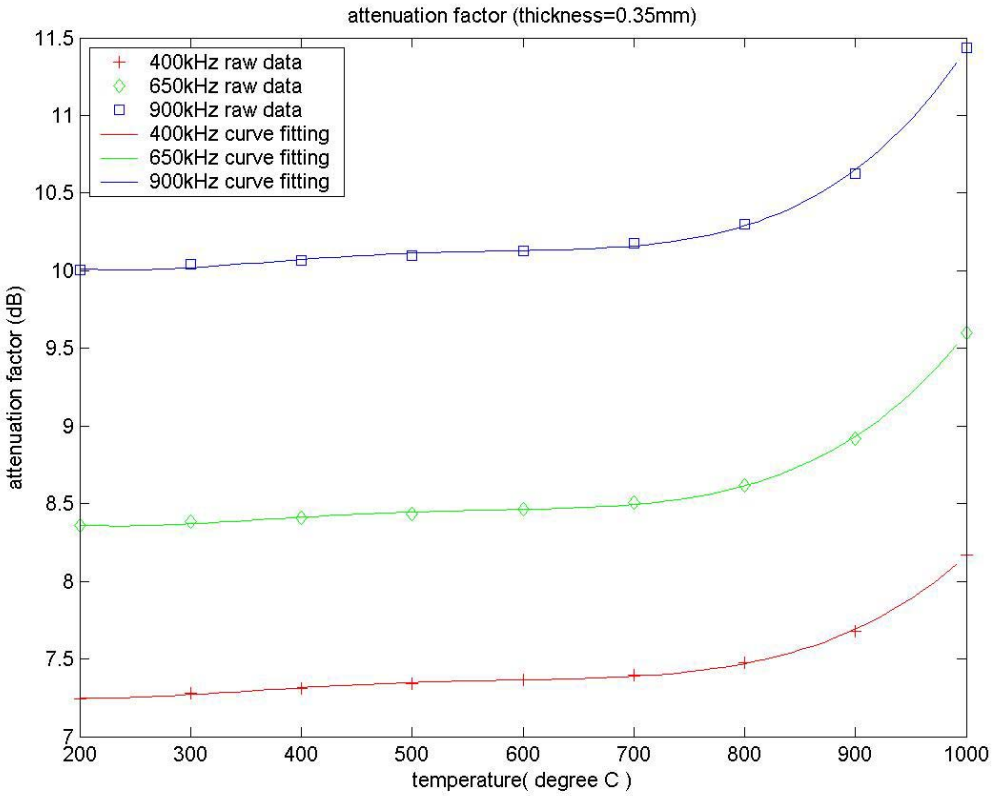

Fig. 5.1b Attenuation factor vs. temperatures for plate thickness=0.35mm

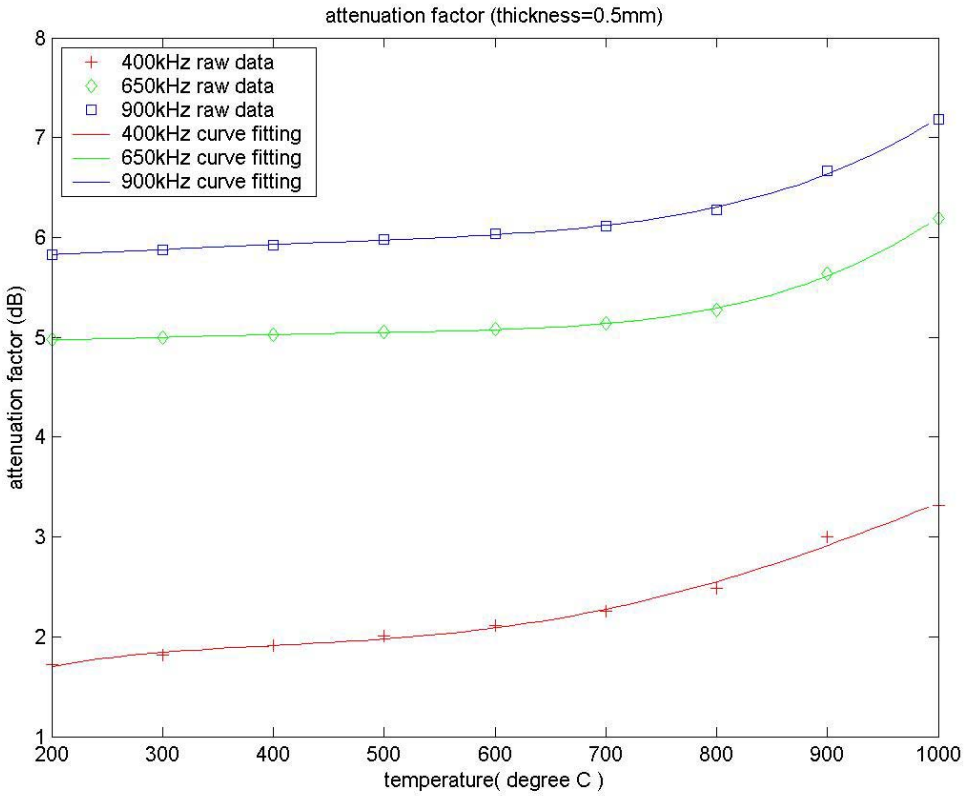

Fig. 5.1c Attenuation factor vs. temperatures for plate thickness=0.5mm

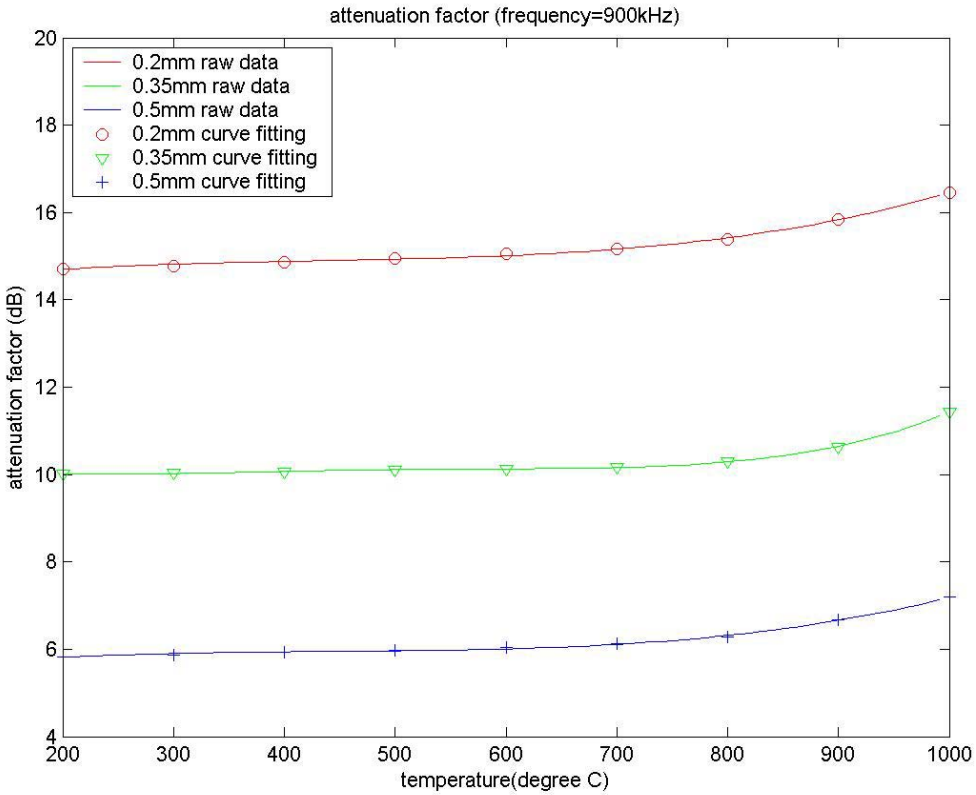

Fig. 5.2 Attenuation factor vs. temperature for 900kHz frequency component

Table 5.1

Attenuation factor change with temperature change of 1°C

Temperature	0.2mm	0.35mm	0.5mm
200°C	0.0016	5.6451e-004	0.0014
400°C	5.1381e-004	5.3022e-004	2.3797e-004
600°C	0.0010	1.3109e-004	6.5568e-004
800°C	0.0033	0.0021	0.0026
1000°C	0.0069	0.0097	0.0059

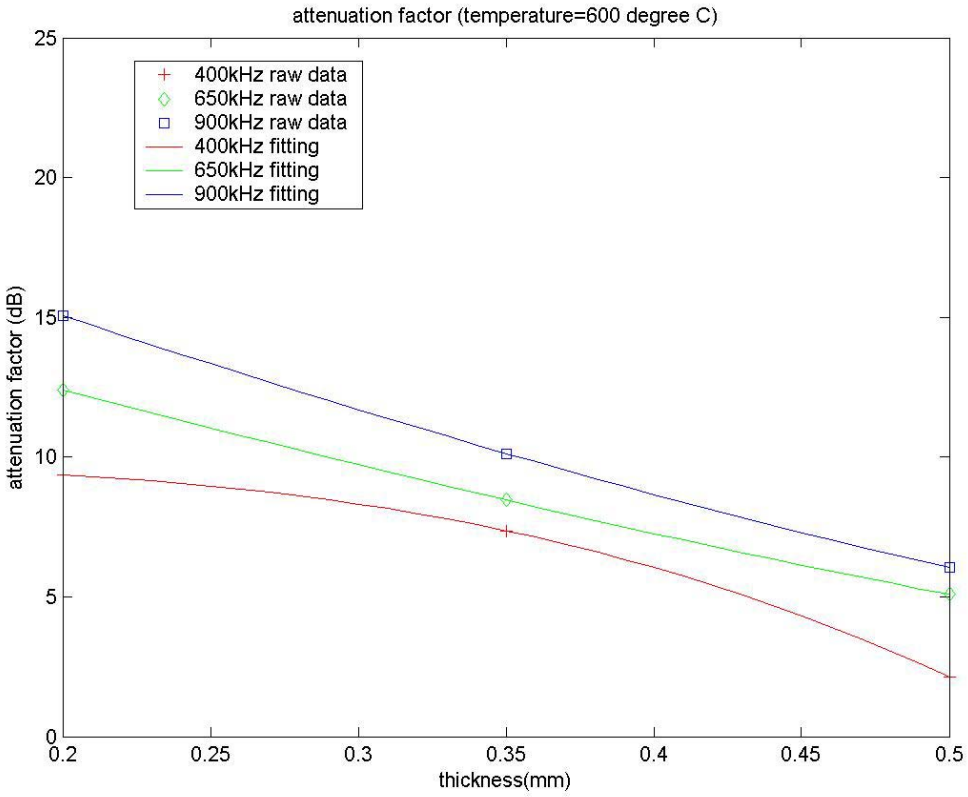

Fig. 5.3a Attenuation factor for different thickness at 600°C

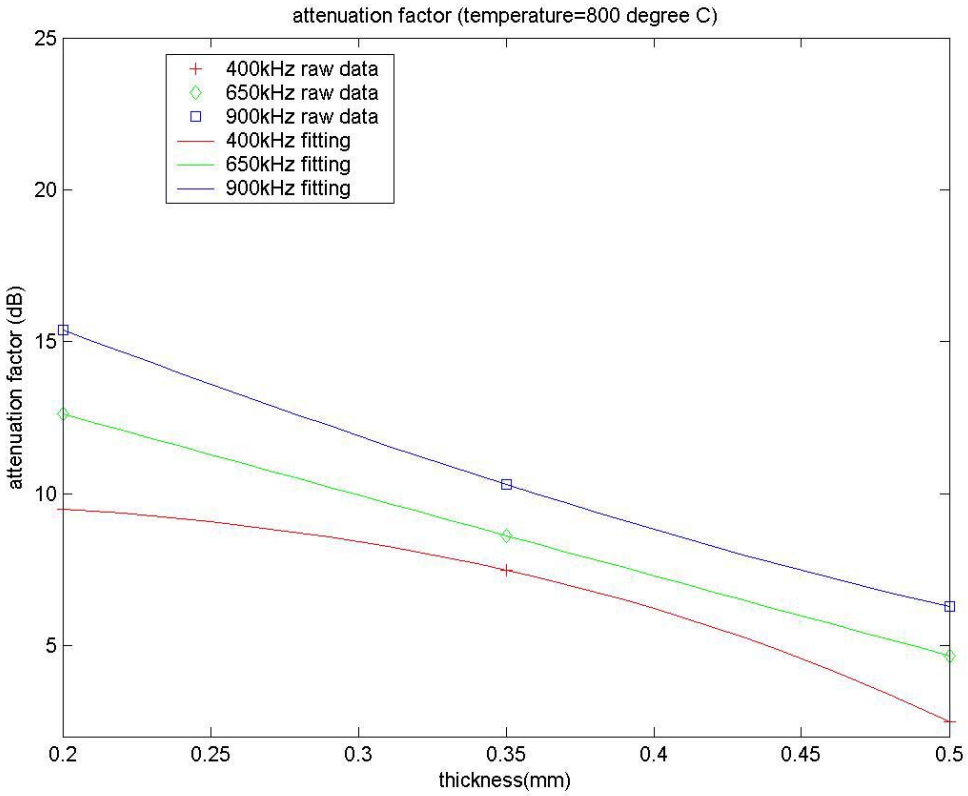

Fig. 5.3b Attenuation factor for different thickness at 800°C

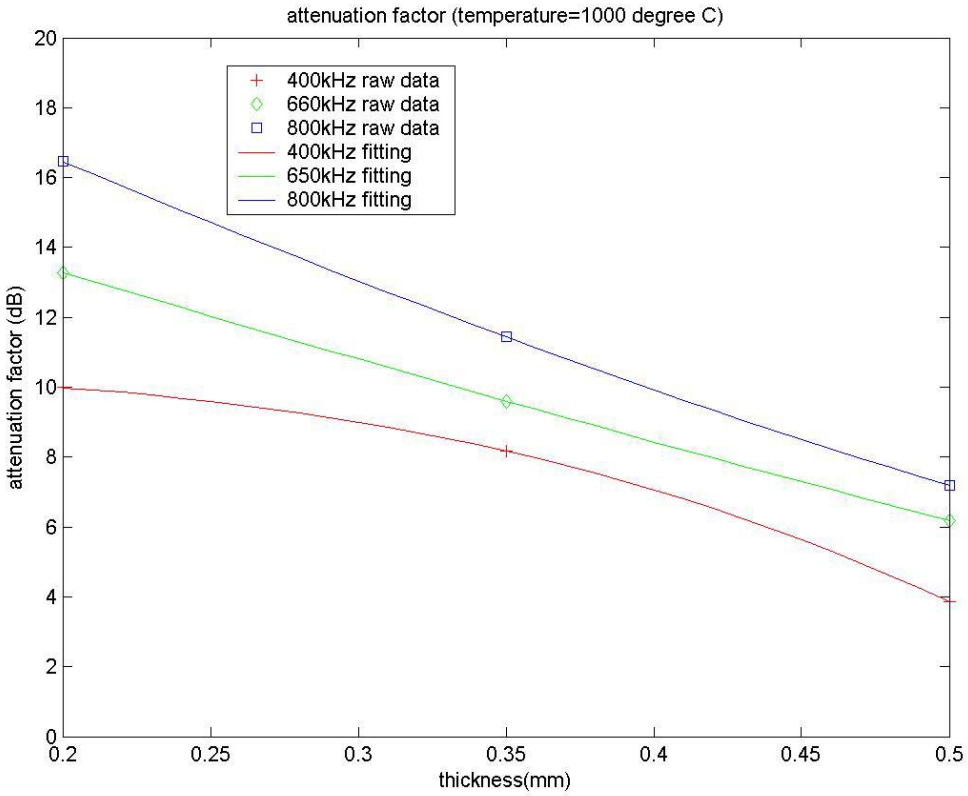

Fig. 5.3c Attenuation factor for different thickness at 1000°C

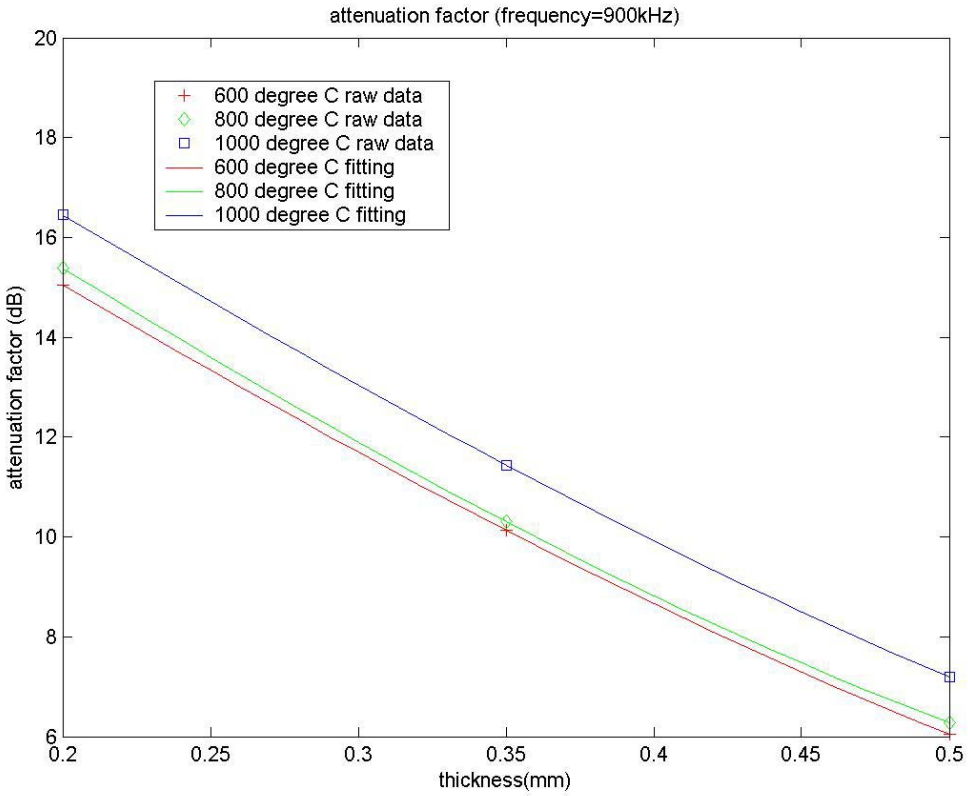

Fig. 5.4 Attenuation factor vs. thickness for 900kHz frequency component

Table 5.2

Attenuation factor change with thickness change of 0.1mm

Thickness	600°C	800°C	1000°C
0.2mm	3.488(dB)	3.651(dB)	3.538(dB)
0.35mm	3.061(dB)	3.108(dB)	3.538(dB)
0.5mm	2.448(dB)	2.329(dB)	2.574(dB)

5.3 Temperature Influence on Wave Dispersion

Group velocity as functions of temperature for three different plate thickness are presented in Fig. 5.5a through Fig. 5.5c. From the figures it can be seen that group velocity changes faster with temperature at low frequency, thus suggesting better temperature resolution at lower frequencies. Also, group velocity as a function of both thickness and temperature becomes prominent for low frequency components. Fig. 5.6 shows the group velocity as a function of temperature at 450kHz. Again, three thicknesses are considered. Table 5.3 shows the change of group velocity caused by 1°C change of temperature at 450kHz. The table can be used to calibrate temperature by wave dispersion. From Table 5.3, it is observed that to achieve the temperature resolution of 1°C, the LISWT technology must be able to discern the change in group velocity at the order of 0.1m/s.

The requirement for LISWT to achieve ±1°C resolution through exploring wave dispersion can be estimated as follows. Assume the distance between the two sampling locations is d (which is 5mm in this study) and the velocity at which a particular frequency component propagates is v. The time-of-flight can be readily calculated as

$$\Delta t = \frac{d}{v} \tag{5.1}$$

Now assume the velocity change is $\Delta v = 0.1 m/s$. This is relatively small change according to Table 5.3, so it sets a relatively high standard for LISWT. The change of Δt caused by this velocity change is therefore

$$\xi = \frac{\Delta v}{v + \Delta v}\Delta t \tag{5.2}$$

Assume the velocity is 3,000m/s. This is a relatively large velocity in the velocity range shown in Table 5.3, so it also sets a relatively high standard for LISWT. These high standard assumptions correspond to two possible worst-case scenarios. According to the above assumptions, the change in the time-of-flight is only 5.56×10^{-11}s. The current LISWT setup is not able to detect such a small change in the time-of-flight.

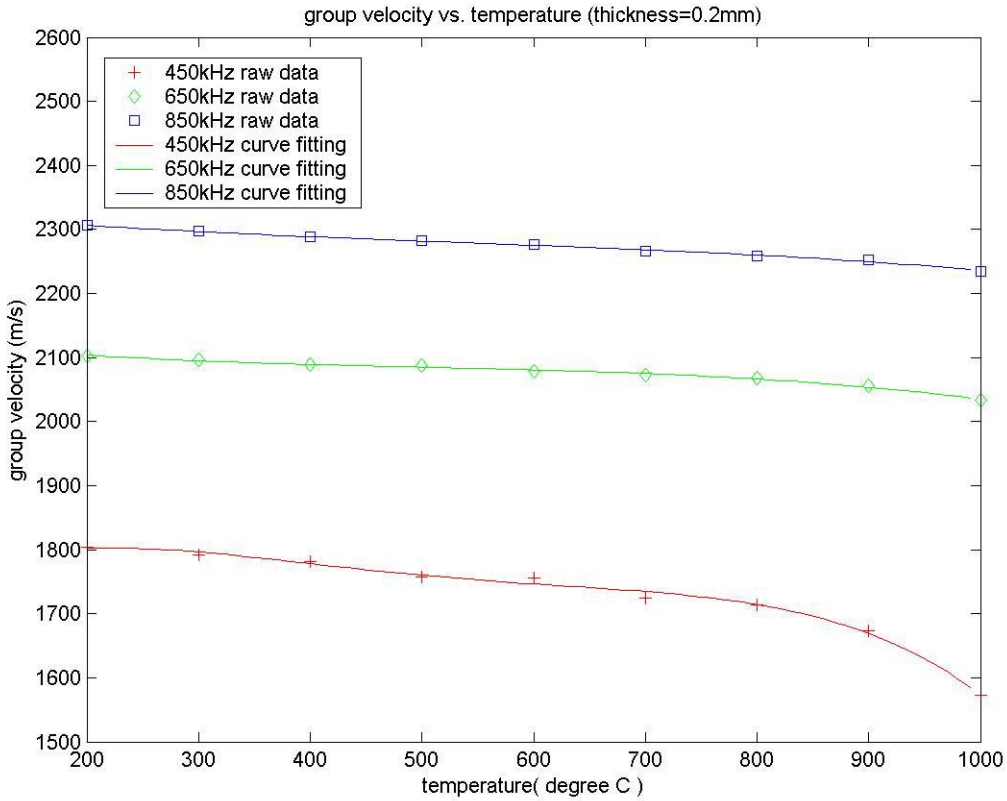

Fig. 5.5a Group velocity vs. temperature for plate thickness=0.2mm

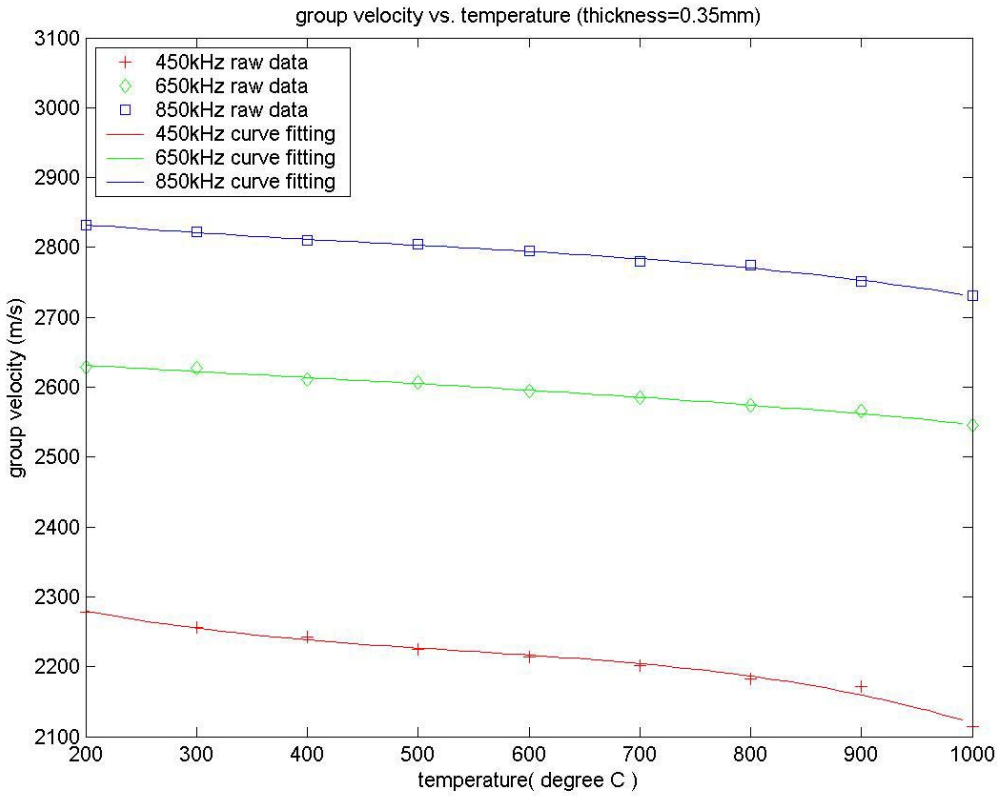

Fig. 5.5b Group velocity vs. temperature for plate thickness=0.35mm

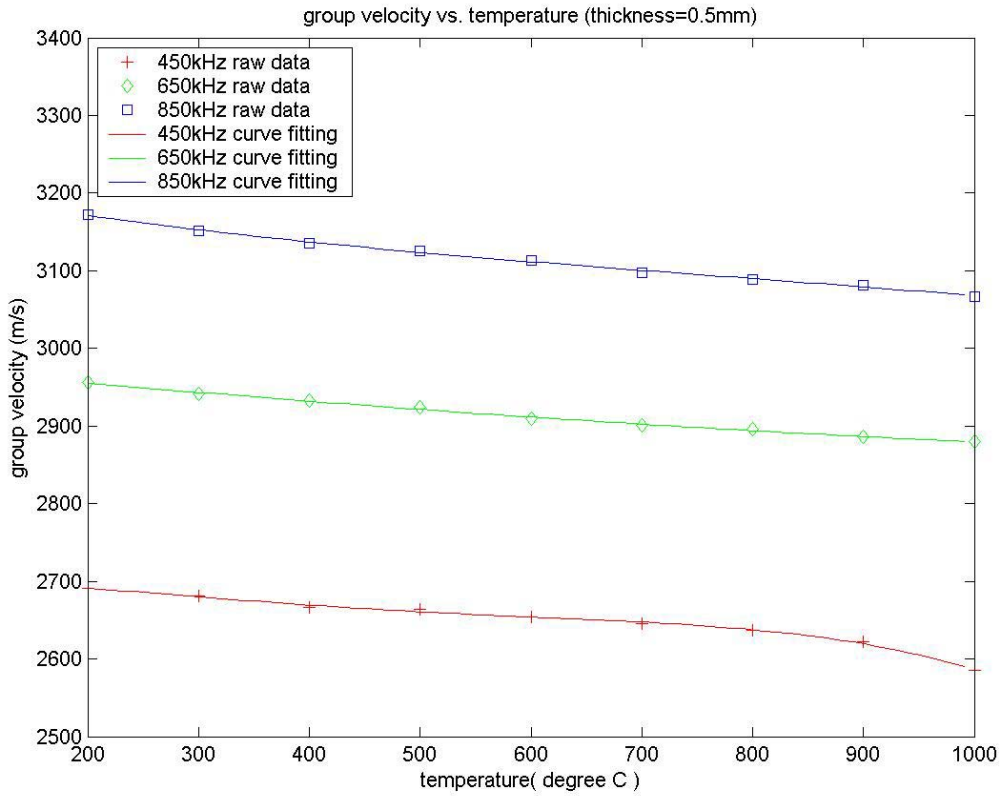

Fig. 5.5c Group velocity vs. temperature for plate thickness=0.5mm

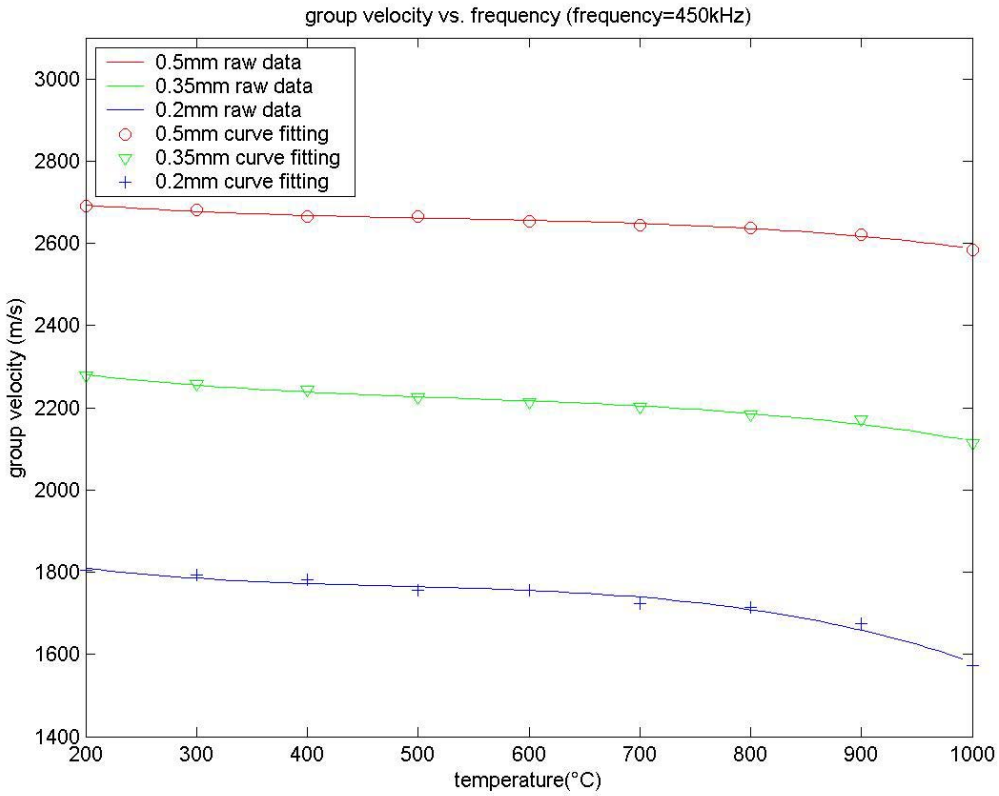

Fig. 5.6 Group velocity vs. temperature for 450 kHz frequency component

Table 5.3

Group velocity change with temperature change of 1°C

Temperature	0.2mm	0.35mm	0.5mm
200°C	0.3267	0.3111	0.1958
400°C	0.0945	0.1374	0.0759
600°C	0.1143	0.1055	0.0609
800°C	0.3858	0.2155	0.1508
1000°C	0.8771	0.4513	0.3332

If a low frequency, low velocity component were used along with a longer propagation path (between the 2 sample locations), to achieve the desired ±1°C resolution becomes probable. Using Fig. 5.5c and considering the low frequency zone, it was found that the group velocity for the 50kHz component is at the order of 300m/s for temperature at 800°C. If the separation between the sampling locations is 100mm, according to Eq. (5.2), the change in the time-of-flight caused by 1°C temperature difference is at the order of 1×10^{-7}s. If the 20kHz frequency is used, the change in the time-of-flight is at the order of 1×10^{-6}s, which is obtainable using the LISWT setup. From the discussion above, it is concluded that the desired ±1°C thermal resolution can be achieved if low frequency components are used to extract thermal information.

5.4 Thickness Influence on Wave Dispersion

The group velocity for different thickness is given in Figs. 5.7a-5.7c. According to these figures, the group velocity varies nonlinearly with thickness. Fig. 5.8 shows the group velocity as a function of thickness at 800kHz. Table 5.4 shows the change of group velocity caused by 0.1mm change in thickness at 800kHz. This table can be used to calibrate thickness by dispersion relation. The influence of thickness on dispersion is non-negligible as shown in Table 5.4. For the LISWT system to detect 0.1mm thickness changes, it must be able to measure velocity changes ranging from 200m/s to 300m/s.

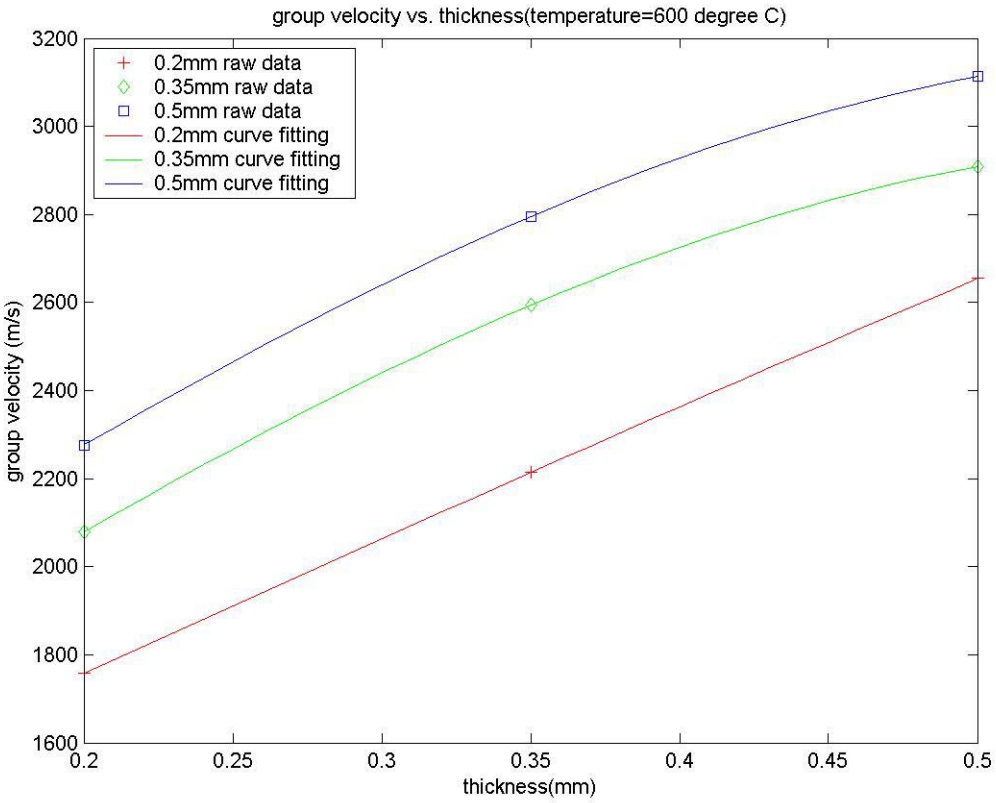

Fig. 5.7a Group velocity vs. thickness (temperature=600°C)

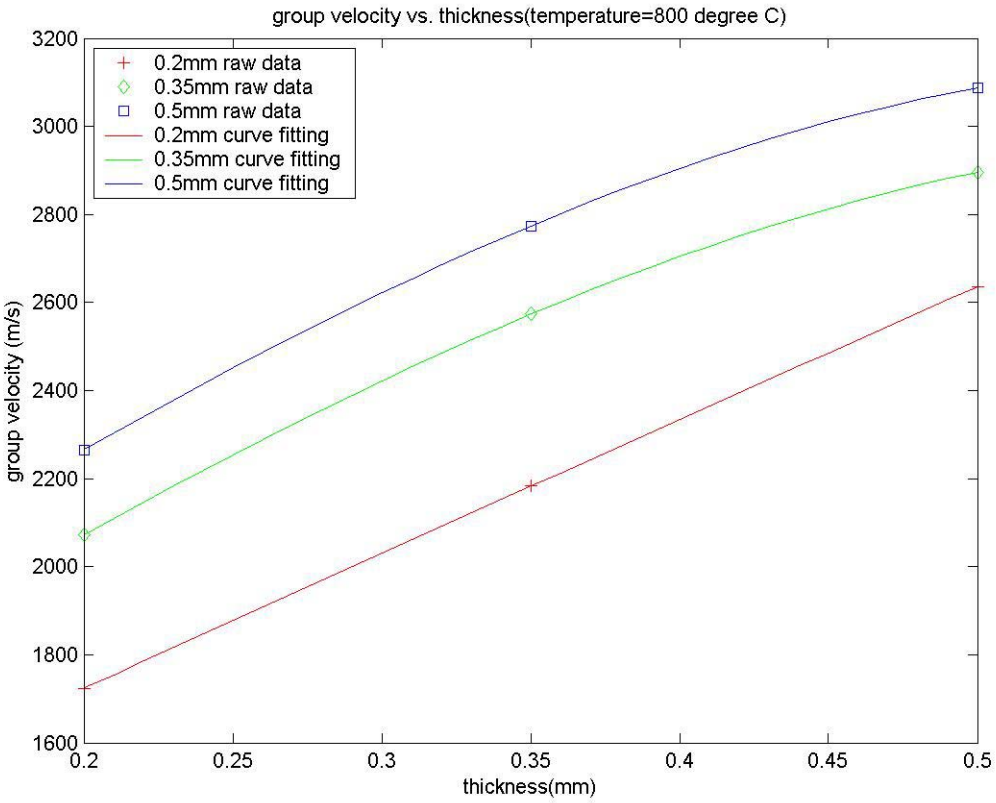

Fig. 5.7b Group velocity vs. thickness (temperature=800°C)

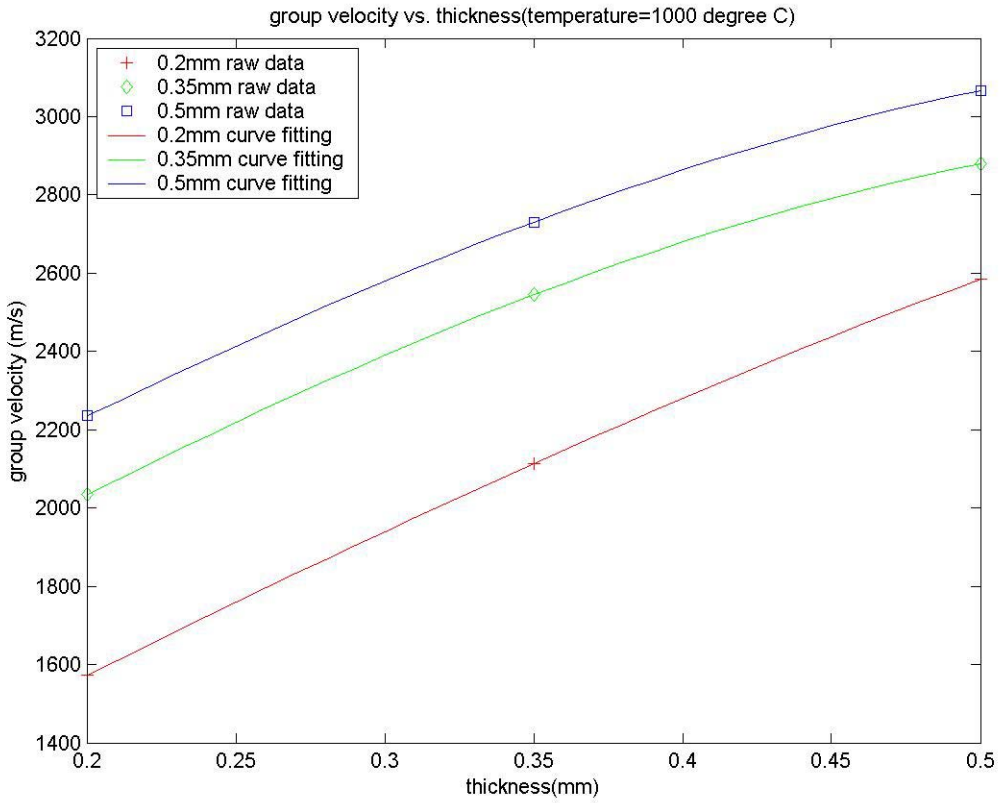

Fig. 5.7c Group velocity vs. thickness (temperature=1000°C)

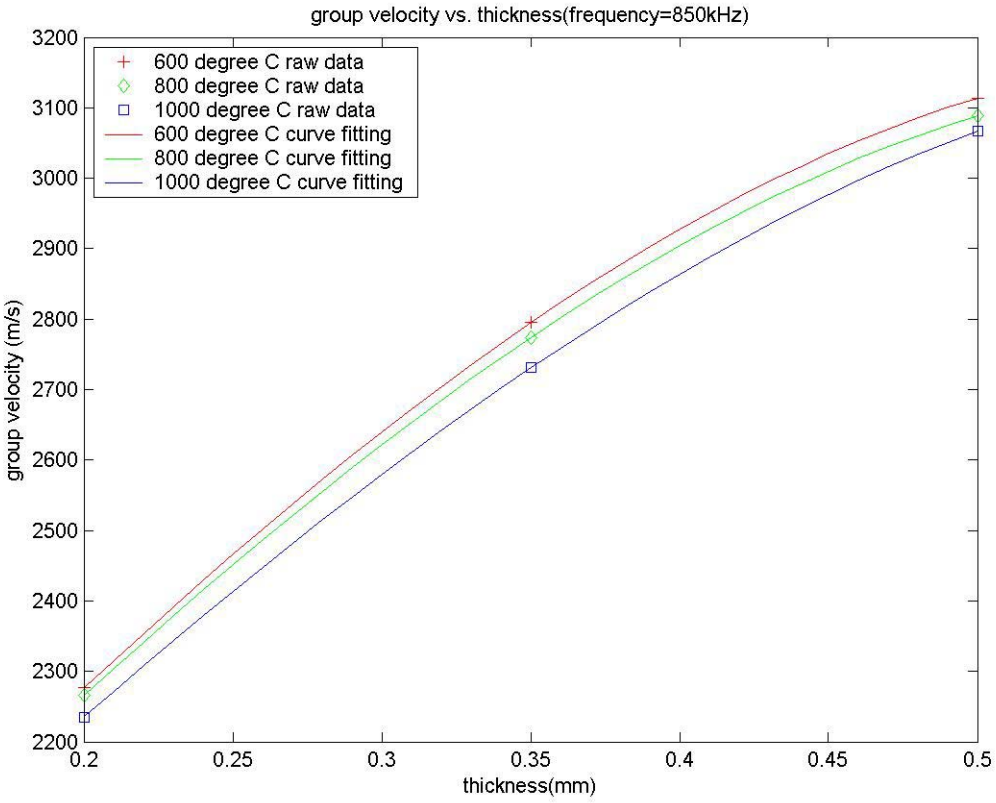

Fig. 5.8 Group velocity vs. thickness (frequency=850kHz)

Table 5.4

Group velocity change with thickness change of 0.1mm

Thickness Range	600°C	800°C	1000°C
0.2mm	395.9(m/s)	387.6(m/s)	370.6(m/s)
0.35mm	293.1(m/s)	287.7(m/s)	370.6(m/s)
0.5mm	145.5(m/s)	144.4(m/s)	170.6(m/s)

5.5 Summary

From the results presented one can conclude that temperature and wafer thickness both have an effect on wave attenuation and dispersion. The influence of temperature is nonlinear. The nonlinearity becomes even more prominent at higher temperatures. Also, higher the frequency, faster the attenuation factor varies with temperature. For every degree change of temperature, the corresponding change in attenuation factor is of the order of 10^{-4}dB to 10^{-3}dB using the (high) 800kHz frequency. For dispersion, the results showed that at lower frequency, group velocity varies faster with temperature. For every degree change of temperature, the corresponding change in group velocity is from 0.1m/s to 1m/s using the 450kHz frequency. To detect 1°C temperature variation, resolutions required for resolving wave attenuation and group velocity are stringent. The change in the time-of-flight caused by 1°C change in temperature is at the order of 10^{-11} s, which is not attainable for the LISWT technology. However, using 20kHz low frequency component and a wave propagation path of 100mm, the desired 1°C temperature resolution can be readily resolved using LISWT system as the change in the time-of-flight is now of the order of 10^{-6}s.

The influence of thickness on wave attenuation and dispersion is much more significant. For attenuation, higher the frequency, faster the attenuation factor increases with thickness. Using 800kHz frequency component, for every 0.1mm change in thickness, the orders of changes in attenuation factor and group velocity are from 1dB to 10dB and from 200m/s to 300m/s, respectively. The current LISWT setup is able to

achieve such a spatial resolution through exploring wave attenuation and dispersion without any enhancement.

CHAPTER VI

CONCLUSIONS AND FUTURE WORK

The primary objective of the thesis is to establish the knowledge base of elasto-viscoplastic wave propagation in silicon wafers at elevated temperature and establish the feasibility of Laser Induced Stress Wave Thermometry (LISWT) for wafer fabrication. While extensive work has been performed on demonstrating the applicability of LISWT to temperatures below 600°C, the feasibility of LISWT at temperatures higher than 600°C remained to be explored. Rapid Thermal Processing (RTP), for which LISWT was developed to provide accurate temperature measurement, has a working temperature range from 25°C to exceeding 1,000°C. The need for verifying that LISWT is valid for all ranges of RTP temperature motivated the work.

To meet the objective, an elasto-viscoplastic constitutive law applicable to the required temperature range was identified and, upon the availability of the constitutive law, an elasto-viscoplastic wave propagation formulation was then derived. As the governing equations were mathematical complicated and tangible analytical solutions seemed unlikely, an explicit staggered grid finite difference scheme was developed for approximating wave solutions. Given the configuration and boundary conditions, elasto-viscoplastic Lamb plate waves were propagated in thin silicon wafers. A Gabor Wavelet Transform (GWT) based method was then applied to analyze the attenuation and dispersion of the waves for thermal information.

Since the fundamental laws of continuum mechanics provide the most generalized description of mechanical motions in nature, the approach for developing theoretical wave propagation model is always the same regardless of the type of wave that is studied. The elasto-viscoplastic waves in silicon wafers were found to be governed by a first-order hyperbolic equation system. The advantage provided by the first-order hyperbolic system is many folds. First it renders possible the incorporation of a complex constitutive law. This is what the conventional displacement (or stress) formulation

cannot handle because elimination of unknowns is impossible with such a complex constitutive law present. Secondly, it enables velocity and stress as the dependent variables. In other words, unlike the conventional formulation where displacement is the unknown to be solved for, it provides a straightforward way to obtain information on both motion and force simultaneously. Finally this first-order system can be readily discretized following the staggered grid method.

The explicit staggered grid finite difference scheme provided efficient solutions to the 3D initial-boundary value problems governed by the first-order hyperbolic equation system. The explicit time discretization eliminated the need for iteratively solving the nonlinear equation system at each time step. The stability problem associated with the explicit time scheme was addressed by choosing a proper time step according to the Courant condition. The staggered grid scheme is a discretization scheme of high accuracy, as compared with the conventional central difference scheme. Variables are defined at different grid points on a finite difference element, or control volume. All numerically generated A_0 and S_0 Lamb wave modes were clearly identified. Numerical convergence was also verified using progressively refined meshes. A C-language program was assembled to implement the numerical scheme. Simulated waveforms were acquired in silicon plates of three different thicknesses at five different temperatures. These waveforms were then analyzed using the aforementioned GWT analysis method for thermal information extraction.

The approach developed for studying wave attenuation employed the projection of GWT on the frequency axis. Since waves studied in the thesis were all dispersive Lamb guided modes, the attenuation factor cannot be defined using Fourier Transform, which is valid only for stationary signals. To maintain logical consistency, GWT was introduced as an alternative to Fourier Transform for decomposing wave signals into their associated frequency components. GWT was primarily for the extraction of wave dispersion. Since successful application of GWT is contingent upon the proper choice of parameter ranges, extensive numerical experiments were performed. Good balance between time and frequency resolution was achieved as a result.

From the results reported herein, it was concluded that wave group velocity is a nonlinear function of temperature. As nonlinearity is even more prominent at higher temperatures, better resolution can be expected if wave dispersion is used for profiling high temperature. Using the 20kHz frequency component, it was demonstrated that for every 1°C variation of temperature, LISWT would need to be able to differentiate changes in the time-of-flight of the frequency as small as 1 microsecond for covering a 100mm propagation path. The influence of thickness was found to be more significant than temperature. 0.1mm in thickness variation resulted in a 200 m/s change in wave group velocity, implying that silicon wafers must be accurately calibrated for thickness variation before temperature measurement should be attempted using LISWT.

This thesis presented a comprehensive work on establishing the knowledge base for the expanded applicability of LISWT and provided a framework within which LISWT can be enhanced to achieve the desired ±1°C resolution with accuracy. The model introduced in the thesis can be easily adapted to account for other nondestructive evaluation applications involving the use of surface, plate or bulk waves.

There are several issues that should be further addressed. Initiation of laser induced thermal and mechanical disturbances is a very involved process. The mechanism behind laser induced thermal-mechanical wave propagation at elevated temperatures was not investigated. Instead of attempting to explore the physics of laser heating, the thesis employed a stress rate input for simplicity. A comprehensive knowledge of this process will require an in-depth understanding of ultra-fast radiation-matter interactions at the scale of molecules. Such knowledge, if available, would also have an impact on laser micromachining and nano-manufacturing. The work presented in the thesis provides the essential foundation upon which laser heating can be built. Also, since what laser induced are coupled thermal-mechanical waves, it is suggested that thermal-elastic and thermal-plastic effects on the silicon constitutive law be further investigated to quantify the influence of thermal wave propagation on attenuation and dispersion. Finally, LISWT needs be enhanced accordingly to validate physically what has been concluded as viable in this thesis.

REFERENCES

[1] The National Technology Roadmap for Semiconductors, Semiconductor Industry Association, San Jose, California 1998.

[2] G.A. Rabroker, C.S. Suh, C.P. Burger, R. Chona, Analytical feasibility of laser induced stress waves thermometry applied to silicon wafers, Proc. of the Symposium on Applications of Experimental Mechanics to Electronic Packaging ASME AMD 226 (1997) 45-50.

[3] Y.J. Lee, B.T. Khuri-Yakub, K.C. Saraswat, Temperature measurement in rapid thermal processing using the acoustic temperature sensor, IEEE Transactions on Semiconductor Manufacturing 9 (1) (1996) 115-121.

[4] C.S. Suh, G.A. Rabroker, R. Chona, and C.P. Burger, Lamb wave propagation as a temperature diagnostic in silicon wafer processing: experimental implementation and results, Proc. of the 1998 SEM Spring Conf. on Experimental Mechanics (1998) 455-458.

[5] C.S. Suh, G.A. Rabroker, C.P. Burger, R. Chona, Ultrasonic time-frequency characterization of silicon wafers at elevated temperatures, Proc. of the Symposium on Application of Experiment Mechanics to Electronic Packaging ASME EEP 22 AMD 226 (1997) 37-44.

[6] C.S. Suh, C.P. Burger, Experimental time-frequency analysis of laser-induced lamb waves, Proc. of the 1997 SEM Spring Conf. on Experimental Mechanics (1997) 279-280.

[7] C.S. Suh, G.A. Rabroker, C.P. Burger, R. Chona, Ultrasonic time-frequency characterization of silicon wafers at elevated temperatures, Proc. of the Symposium on Application of Experimental Mechanics to Electronic Packaging, ASME, EEP 22 AMD 226 (1997) 37-44.

[8] V. Vedantham, In-Situ temperature and thickness characterization for silicon wafers undergoing thermal annealing, MS Thesis, Texas A&M University (2003).

[9] E.H. Lee, D.T. Liu, Finite-strain elastic-plastic theory with application to plane-wave analysis, Journal of Applied Physics 38 (1) (1967) 19-27.

[10] G. Giese, M. Fey, High-order simulation of the elastic-plastic wave equation in two space dimensions, Wave Motion 38 (2003) 327-343.

[11] H. Alexander, P. Haasen, Dislocation and plastic flow in the diamond structure, Solid State Physics 22 (1968) 28-156.

[12] M. Suezava, K. Sumino, I. Yonenaga, Dislocation dynamics in the plastic deformation of silicon crystals, II. Theoretical analysis of experimental results, Physi. Stat. Sol. a 51 (1979) 217-226.

[13] C. Tsai, O.Dillon, R. Angelis, The constitutive equation for silicon and its use in crystal growth modeling, Journal of Engineering Materials and Technology 112 (1990) 183-187.

[14] W. Recker, A numerical solution of three-dimensional problems in dynamic elasticity, Transactions of the ASME, March (1970) 116-122.

[15] Cerveny V., I. Moloktov, and I. Psencik, Ray method in seismology, Charles Univ. Press, Prague (1977).

[16] J. Virieux, P-SV Wave propagation in heterogeneous media: velocity-stress finite-difference method, Geophysics 51 (4) (1986) 889-901.

[17] J. Robertson, J. Blanch, W. Symes, Viscoelastic finite-difference modeling, Geophysics 59 (9) (1994) 1444-1456.

[18] E. Saenger, N. Gold, S. Shapiro, Modeling the propagation of elastic waves using a modified finite-difference grid, Wave Motion 31 (2000) 77-92.

[19] D. Kosloff, M. Reshef, D, Loewenthal, Elastic wave calculations by the Fourier method: Bull. Seis. Soc. Am. 74 (1984) 875-891.

[20] D. Kosloff, M. Reshef, M. Edwards, and C. Hsiung, Elastic 3-D forward modeling by the Fourier method: 55th Ann. Internat. Mtg. Soc. Explor. Geophys.

[21] H. Tal-Ezer, Spectral methods in time for hyperbolic problems: SIAM J. Numerical Analysis 23 (1986) 11-26.

[22] J. Kole, Solving seismic wave propagation in elastic media using the matrix exponential approach, Wave Motion 38 (2003) 279-293.

[23] Y. Chen, W. Chew, Q. Liu, A three-dimensional finite difference code for the modeling of sonic logging tools, Journal of Acoustic Society of America 103 (2) (1998) 702-712.

[24] Q. Liu, E. Schoen, F. Daube, C. Randall, H, Liu, P. Lee, A three-dimensional finite difference simulation of sonic logging, Journal of Acoustical Society of America 100 (1) (1996) 72-79.

[25] J. Represa, C. Pereira, M. Panizo, F. Tadeo, A simple demonstration of numerical dispersion under FDTD, IEEE Transactions on Education 40 (1) (1997) 98-102.

[26] M. Noriyuki, U. Hitoshi, M. Tsuyoshi, F Kazumasa, S Yuji, Dislocation density analysis of bulk single silicon crystal growth using dislocation kinetics model, AMD-vol.195, Mechanics and Materials for Electronic Packaging, vol. 1- Design and Process Issues in Electronic Packaging, ASME (1994) 59-64.

[27] M. Yasutake, M. Umeno, H Kawabe, Mechanical properties of heat-treated CZ-Si wafers from brittle to ductile temperature range, Japan Journal of Applied Physics 21 L288-90 (1982).

VITA

Li Liu was born on November 5th, 1974 in Hubei, China. He received a Bachelor of Engineering degree in Automotive Engineering from Tsinghua University, Beijing, China in July 1996 and a Master of Engineering degree in Vehicle Engineering from Tsinghua University in July 1999. He was a development engineer at the Research and Development Center (RDC) of ZF Shanghai Steering Company in Shanghai, China, from July 1999 to July 2000. He received his Master of Science degree in Mechanical Engineering from Texas A&M University in May 2005. His permanent address in China is Chao Wai Jin Tai Li, 13-1-502, Beijing, China 100026. He can be reached via email at solidwave@gmail.com.